A novel regulatory mechanism of actin cytoskeleton dynamics through a neural microexon in DAAM1 is important for proper memory formation

Patryk Poliński [1,9], Marta Miret Cuesta [1,8], Alfonsa Zamora-Moratalla [1,8], Federica Mantica [1], Gerard Cantero-Recasens [1,2], Davide Normanno [1,3], Luis Iñiguez Rabago [1], Cruz Morenilla-Palao [4], Patricia Ordoño [4], Sophie Bonnal [1], Raúl Gómez Riera [1], María Martínez De Lagrán Cabredo [1], Álvaro Fernández-Blanco [1], Cristina Rodríguez-Marin [1], Jon Permanyer [1], Orsolya Fölsz [1], Cesar Sierra [1], Diana Legutko [5], José Wojnacki[1], Juan Luis Musoles Lleo [1], Eloisa Herrera [4], Mara Dierssen [1,9], and Manuel Irimia [1,6,7,9]

1 - Centre for Genomic Regulation, Barcelona Institute of Science and Technology, Barcelona, Spain.
2 - Vall d'Hebron Research Institute (VHIR), Barcelona, Spain
3 - Institute of Human Genetics, Université Montpellier, CNRS, Montpellier, France
4 - Instituto de Neurociencias (CSIC-UMH), Alicante, Spain.
5 - Nencki Institute of Experimental Biology, BRAINCITY, Warsaw, Poland
6 - Universitat Pompeu Fabra, Barcelona, Spain.
7 - ICREA, Barcelona, Spain.
8 - Co-second authors.
9 - Corresponding authors.

Patryk Poliński
Centre for Genomic Regulation
Dr. Aiguader, 88, 08003 Barcelona, Spain
e-mail: patrykpolinski@gmail.com
Phone: +34933160213, Fax: +34933160099

Mara Dierssen
Centre for Genomic Regulation
Dr. Aiguader, 88, 08003 Barcelona, Spain
e-mail: mara.dierssen@crg.eu
Phone: +34933160140, Fax: +34933160099

Manuel Irimia
Centre for Genomic Regulation
Dr. Aiguader, 88, 08003 Barcelona, Spain
e-mail: mirimia@gmail.com
Phone: +34933160212, Fax: +34933160099

Abstract

Actin cytoskeleton dynamics is crucial for neurogenesis and neuronal function. Precise quantitative and qualitative regulation of actin polymerization is achieved by multiple actin-binding proteins, among which formins are particularly versatile. Here, we investigate how neuronal-specific splicing expands formin's functional diversity in the brain. We uncovered a highly conserved microexon in DAAM1, whose inclusion extends the linker region of the FH2 domain, and leads to remarkable changes in actin polymerization rates and structure. Microexon deletion causes neuritogenesis defects and increased calcium influx in in vitro differentiated neurons, and mice carrying this deletion exhibit deficient memory formation. These memory defects were associated with higher activity of DAAM1's interactor RhoA, increased ARC protein levels, postsynaptic deficiencies, fewer dendritic spines and impaired long-term potentiation. In summary, precise post-transcriptional regulation of DAAM1's FH2 domain is a novel mechanism for modulating actin dynamics in neurons, and is essential for proper brain function.

Keywords: Alternative splicing, actin, formin, DAAM1, memory formation

Introduction

The higher cognitive functions of mammalian brains are the result of complex interactions among millions of neuronal cells, which are mediated by intercellular connections called synapses. These connections require the development of specialized cellular structures in the presynapse, responsible for the proper storage and turnover of synaptic vesicles filled with neurotransmitters, and in the postsynapse, which receives these signals mainly in the dendritic spines. The precise organization of both the pre- and postsynaptic terminals is to a great extent dependent on the actin cytoskeleton (Cingolani and Goda 2008). At the presynapse, actin networks are responsible for the spatial segregation and cycling of synaptic vesicles (Dillon and Goda 2005; Papandréou and Leterrier 2018), while in the postsynaptic terminals they drive spine morphology and receptor mobility (Cingolani and Goda 2008). As a result, the actin cytoskeleton is crucial for multiple brain functions, including memory formation. For example, actin dynamics directly affects experience-dependent plasticity, which induces specific connectivity patterns between the synapses (Lamprecht 2021; McLeod and Salinas 2018).

The dynamics and structure of the actin cytoskeleton are controlled by many actin-binding proteins (ABPs), whose classification depends mainly on their mode of action. Among them, actin nucleating proteins are both the most important drivers of actin dynamics and the most heterogeneous group of ABPs (Mattila and Lappalainen 2008). They consist of (i) the WH2-containing nucleators; (ii) the Arp2/3 complex, responsible for actin branching; and (iii) the formins, which nucleate linear filament formation and elongation (Pollard 2016). Formin proteins are particularly diverse and versatile, with 15 members grouped into seven families in humans (Schönichen and Geyer 2010). All of them are characterized by a conserved Formin-homology-2 (FH2) domain that forms homodimeric structures directly responsible for processive polymerization of F-actin filaments (Kühn and Geyer 2014; Yamashita et al. 2007; Gao and Chen 2010). The FH2 domain-based "tethered dimer" exists at two states in equilibrium that allow either actin binding or dissociation. Importantly, the interconversion between these two states occurs through the dynamic expansion of the FH2 ring, and it is possible thanks to the high flexibility provided by the linker region (Schönichen and Geyer 2010; Yamashita et al. 2007).

Alternative splicing, the differential processing of exons and introns in eukaryotic genes, is one of the main mechanisms allowing diversification and specialization of protein function. Nearly 95% of human multi-exonic genes undergo alternative splicing (Pan et al. 2008; Wang et al. 2008), and its prevalence is particularly high in mammalian brains (Barbosa-Morais et al. 2012). Neural-specific alternative splicing is highly conserved throughout vertebrate evolution (Barbosa-Morais et al. 2012), and its misregulation underlies major neurodevelopmental disorders (Feng and Xie 2013). An extreme example of this is provided by microexons, very short exons with tight neural-specific expression, exceptional evolutionary conservation, and links to autism spectrum disorder and intellectual disabilities (Irimia et al. 2014; Quesnel-Vallières et al. 2016; Parras et al. 2018; Gonatopoulos-Pournatzis et al. 2018; 2022). So far, only a handful of microexons have been studied in detail, mostly in connection with neurite outgrowth or neuronal activity (Gonatopoulos-Pournatzis and Blencowe 2020). Interestingly, genes harboring neuronal microexons are strongly enriched in functions related to actin filament organization, actin filament-based processes and cytoskeletal protein binding (Irimia et al. 2014; Quesnel-Vallières et al. 2016). However, the impact of microexon inclusion on actin-related neuronal processes remains elusive.

In this study, we assessed the impact of neural-specific alternative splicing on formin proteins and actin cytoskeleton dynamics. Among all formin genes, we identified a highly conserved and neuronal-specific microexon in DAAM1 that uniquely impacts its FH2 domain, modifying the length of its linker region. Using biochemical assays and TIRF microscopy we showed that the inclusion/skipping of the microexon modulates actin polymerization dynamics and structure in vitro. Moreover, its correct inclusion during neuronal differentiation is important for proper neuronal function, since its deletion in in vitro differentiated glutamatergic neurons resulted in increased activity of RhoA, higher basal levels of ARC protein, and augmented Ca2+ influx upon depolarization. In line with these results, microexon removal in vivo led to multiple behavioral abnormalities in postnatal and adult mice, including memory defects that were associated with altered dendritic spine morphology and decreased LTP.

Results

DAAM1 harbors a highly conserved neural-specific microexon within its FH2 domain

To investigate the contribution of alternative splicing to the functional specialization of actin polymerization and nucleation in mammalian neurons, we focused on the family of formins, comprising 15 genes in mammals. Using data from VastDB (Tapial et al. 2017), we found that these genes were widely expressed across cell and tissue types, and eleven of them showed substantial levels of expression (TPM ≥ 10) in brain samples (Figure 1a). Moreover, seven of them increased their expression during neuronal differentiation, Disheveled-associated activator of morphogenesis 1 (Daam1) showing the highest absolute expression in neurons (Figure 1a, right panel). At the level of alternative splicing, we identified six exons in four formin genes with different levels of neural-specific splicing regulation (Figures 1b,c; see Methods) and evolutionary conservation across vertebrates (Figure 1d). In terms of protein impact, one of these exons was predicted to disrupt the open reading frame upon inclusion (FMNL3), two were second-to-last exons containing stop codons giving rise to alternative C termini (FMNL1-B and FMNL2-B), and three corresponded to microexons that preserve the open reading frame (DAAM1, FMNL1-A and FMNL2-A)(Figure 1b). As generally described for microexons (Irimia et al. 2014), these three fall either within a structured domain (i.e., the FH2 domain in DAAM1) or immediately next to it (i.e., the GTPase-binding domain in FMNL1 and the FH2 domain in FMNL2) (Figure 1b).In particular, the microexon in DAAM1 lies within the linker region of the FH2 domain and modifies its length (Figure 1e), which has been reported to have a major impact on actin polymerization (Yamashita et al. 2007). Protein alignments of the FH2 domain of DAAM1 and its linker region across vertebrates revealed that the microexon has been conserved at the orthologous position from sharks to humans, keeping a constant length of 9-10 amino acids (Figure 1f). Moreover, transcriptomic data from various vertebrate species available in VastDB (Tapial et al. 2017) showed that inclusion of the microexon in DAAM1 is also tightly restricted to neural tissues in other vertebrates (Figure 1g). This inclusion pattern was validated using RT-PCR assays in mouse and zebrafish tissues (Figure 1h). Additionally, in line with previous studies (Calarco et al. 2009; Raj et al. 2014), we found that the inclusion of the microexon was highly dependent on the action of SRRM3/4 in humans, mice and zebrafish (Figure 1i). Because of its higher neural-specificity and evolutionary conservation compared to other formin alternative exons, and its direct impact on the FH2 domain, we decided to focus on the microexon of DAAM1 (hereafter Daam1-MIC).

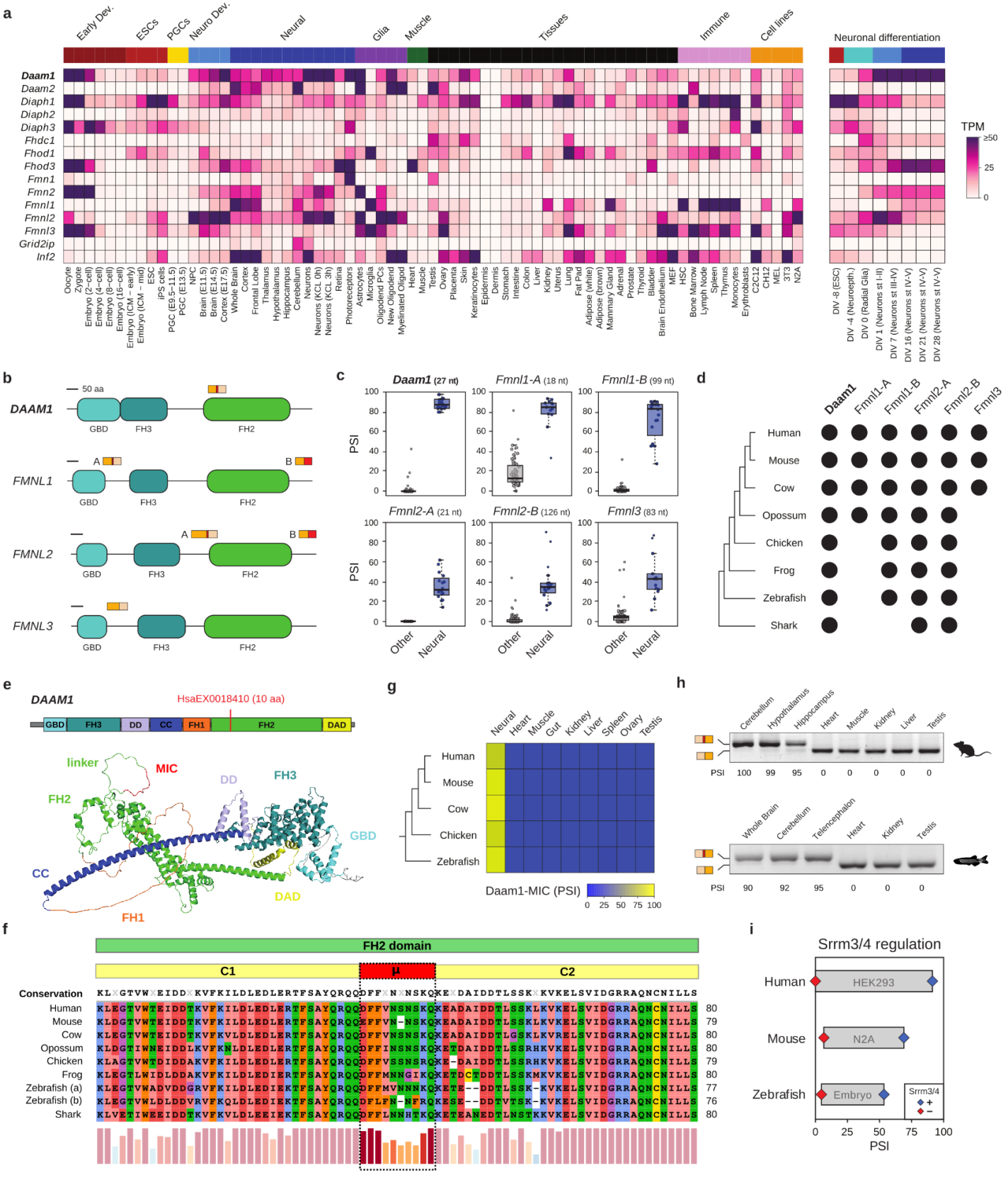
a
Early Dev.
ESCs
PGCs
Neuro Dev.
Neural
Glia
Muscle
Tissues
Immune
Cell lines
Neuronal differentiation
Daam1
Daam2
Diaph1
Diaph2
Diaph3
Fhdc1
Fhod1
Fhod3
Fmn1
Fmn2
Fmnl1
Fmnl2
Fmnl3
Grid2ip
Inf2
TPM
≥50
25
0
b
DAAM1
FMNL1
FMNL2
FMNL3
50 aa
GBD
FH3
FH2
A
B
c
Daam1 (27 nt)
Fmnl1-A (18 nt)
Fmnl1-B (99 nt)
Fmnl2-A (21 nt)
Fmnl2-B (126 nt)
Fmnl3 (83 nt)
PSI
Other
Neural
d
Daam1
Fmnl1-A
Fmnl1-B
Fmnl2-A
Fmnl2-B
Fmnl3
Human
Mouse
Cow
Opossum
Chicken
Frog
Zebrafish
Shark
e
DAAM1
HsaEX0018410 (10 aa)
GBD
FH3
DD
CC
FH1
FH2
DAD
linker
MIC
g
Neural
Heart
Muscle
Gut
Kidney
Liver
Spleen
Ovary
Testis
Daam1-MIC (PSI)
h
Cerebellum
Hypothalamus
Hippocampus
Heart
Muscle
Kidney
Liver
Testis
PSI
100
99
95
0
0
0
0
0
Whole Brain
Cerebellum
Telencephalon
Heart
Kidney
Testis
90
92
95
0
0
0
f
FH2 domain
C1
μ
C2
Conservation
Human
Mouse
Cow
Opossum
Chicken
Frog
Zebrafish (a)
Zebrafish (b)
Shark
i
Srrm3/4 regulation
Human
Mouse
Zebrafish
HEK293
N2A
Embryo
Srrm3/4
PSI

Figure 1 - Neuronal-specificity and evolutionary conservation of Daam1-MIC. (a) Heatmap showing gene expression levels of formin genes across multiple tissues and cell types based on VastDB. TPM: Transcript Per Million. (b) Schematic representation of the protein impact of neural-specific exons. (c) Distribution of inclusion levels, using the Percent Spliced In (PSI) metric, for neural-specific exons in formin genes. PSI values were obtained from VastDB. (d) Evolutionary conservation of neural-specific alternative exons in formin genes. Black dots indicate the presence of an exon ortholog at the genome-level. (e) Schematic representation of DAAM1 and its domains (top), together with DAAM1 protein structure based on AlphaFold2 (bottom). The location of Daam1-MIC (HsaEX0018410 in VastDB) is shown. GBD, GTPase-binding domain; FH3, Formin-Homology-3 domain or Diaphanous-Inhibitory Domain; DD, Dimerization Domain; CC, Coiled-Coil Domain; FH1, Formin-Homology-1 domain; FH2, Formin-Homology-2 domain; DAD, Diaphanous-Autoregulatory Domain. (f) Partial amino acid sequence alignment of the FH2 domain of DAAM1 orthologs across vertebrates. Microexon (μ), upstream (C1), and downstream exons (C2) are indicated. Barplot depicts amino acid conservation. (g) Conserved neural-specificity of Daam1-MIC orthologs in vertebrates. PSI values from VastDB. (h) RT-PCR assays showing the inclusion of Daam1-MIC orthologs in different tissues from mice and zebrafish. Inclusion and the skipping bands are indicated on the left side of the gel. PSI values are indicated below. (i) Srrm3/4-dependent regulation of Daam1-MIC orthologs in human, mouse and zebrafish. PSI values in the condition with (+, blue) or without (-, red) Srrm3/4 is shown. RNA-seq data from human HEK293 cells overexpressing human SRRM4 (Torres-Méndez et al. 2019), mouse N2A cells upon Srrm3/4 knockdown (Gonatopoulos-Pournatzis et al. 2018), and zebrafish retinae extracted from Srrm3 KO 5 days post fertilization larvae (Ciampi et al. 2022).

Daam1-MIC extends the FH2 linker region impacting actin polymerization and structure

To gain further insights into the functional impact of Daam1-MIC, we next generated models of the core structure of DAAM1's FH2 domain (Figure 2a) for the inclusion and skipping variants. These models suggest that the microexon is inserted into the disordered linker region of FH2 without causing major structural changes (red, Figure 2b). The linker region is responsible for both the flexibility of the FH2 domain and its processive polymerization of actin (Otomo et al. 2005). Interestingly, a comparative analysis among human formin proteins revealed that the insertion of the ten amino acids encoded by the microexon makes the linker of DAAM1 the longest among all formins (Figures 2c,d and S1a). Therefore, since the length of the linker is associated with the activity levels of DAAM1 (Yamashita et al. 2007), we hypothesized that the microexon insertion modulates DAAM1-mediated actin polymerization specifically in neurons.

To test this hypothesis and assess how the microexon insertion affects actin polymerization, we first purified the C-terminal part of the human DAAM1 protein with and without the microexon (Figure 2a). This region (FH2-COOH) encompasses the full FH2 domain and has been previously shown to be functional in vitro (Lu et al. 2007). After testing different actin and DAAM1 concentrations to select the optimal conditions for the experiment (Figure S1b-d), we compared the actin assembly activities of both splice isoforms. Remarkably, the isoform without microexon (FH2-COOH (-MIC)) exhibited a significantly higher actin polymerization rate (Figure 2e,f). These results are in line with a previous study showing that random shortening of the linker region increased DAAM1's actin polymerization activity (Yamashita et al. 2007).

To further characterize the impact of Daam1-MIC in actin dynamics and structure, we performed Total Internal Reflection Fluorescence (TIRF) microscopy experiments to directly visualize the actin network, which revealed a more complex picture of the functional differences between the two isoforms (Figures 2g and S2a). Consistent with the previous polymerization experiments, the skipping isoform exhibited an overall higher actin polymerization activity, as assessed by total intensity quantification (Figure S2b). Moreover, TIRF experiments showed that the difference between the two isoforms was not solely in polymerization activity, but they also had a qualitatively different behavior resulting in distinct organizations of the actin network (Figures 2g and S2a-c). Detailed comparison of the spatio-temporal evolution of the actin network's morphology at the level of individual fibers (i.e., bundles of actin filaments) showed that the microexon-containing isoform led to a higher average length of the actin fibers (Figure S2e) and of their individual branches (Figure S2f), with a trend to increase crossing junctions between fibers (Figure S2g) resulting in the formation of multiple branches (Figure S2h). Therefore, Daam1-MIC inclusion leads to an overall more complex network topology in these assays.

Previous studies also suggested that DAAM1 is a potent actin-bundling protein (Jaiswal et al. 2013). Remarkably, microexon removal resulted in significantly higher fiber fluorescence, pointing at higher filament bundling activity for this isoform (Figures 2h and S2i). This suggests that the splice variants of DAAM1 interact with actin differently, in terms of kinetics and/or affinity, which could explain the different behaviors described above. Thus, we next investigated whether the inclusion and skipping isoforms exhibited differences in binding to actin fibers. To do so, we performed dual-color TIRF microscopy experiments using SNAP-tagged DAAM1 FH2-COOH fragments (Figure S3a-c). Both SNAP-tagged protein isoforms showed strong co-localization with actin fibers (Figure 2i and S3d). However, analysis of individual actin bundles revealed a significantly higher amount of skipping isoform bound to actin fiber (Figure 2i,j and S3e). This is likely due to the intrinsic activity of the isoform, as no major differences in dimerization ability were observed between the two isoforms based on the FPLC profiles (Figure S3a). In summary, these results demonstrate that microexon inclusion has a strong impact on the functionality of the FH2 domain of DAAM1, quantitatively and qualitatively. Microexon skipping increases actin bundling while its inclusion promotes actin fiber elongation and dynamic turnover, resulting in a different organization of the actin network.

Daam1-MIC deletion leads to altered neuronal excitability in glutamatergic neurons

To begin investigating the relevance of Daam1-MIC in neuronal differentiation and function, we deleted the microexon in mouse embryonic stem cells (ESCs) using the CRISPR-Cas9 system (see Methods). We selected three independent KO and control ESC clones and differentiated them in vitro into glutamatergic neurons (Figure 3a) (Bibel et al. 2004; 2007). RT-PCR assays confirmed the precise microexon deletion in KO cells, with no associated mis-splicing along differentiation, whereas control cells displayed prominent microexon inclusion soon after plating of neuronal precursor cells (DIV0) (Figures 3b and S4a).

Since DAAM proteins have been shown to be important for neurite morphology and filopodia integrity (Jaiswal et al. 2013; Matusek et al. 2008; Szikora et al. 2017), we first assessed the impact of the microexon removal on filopodia formation and neurite morphology at early stages of neuronal differentiation (Figure S4b). Daam1-MIC

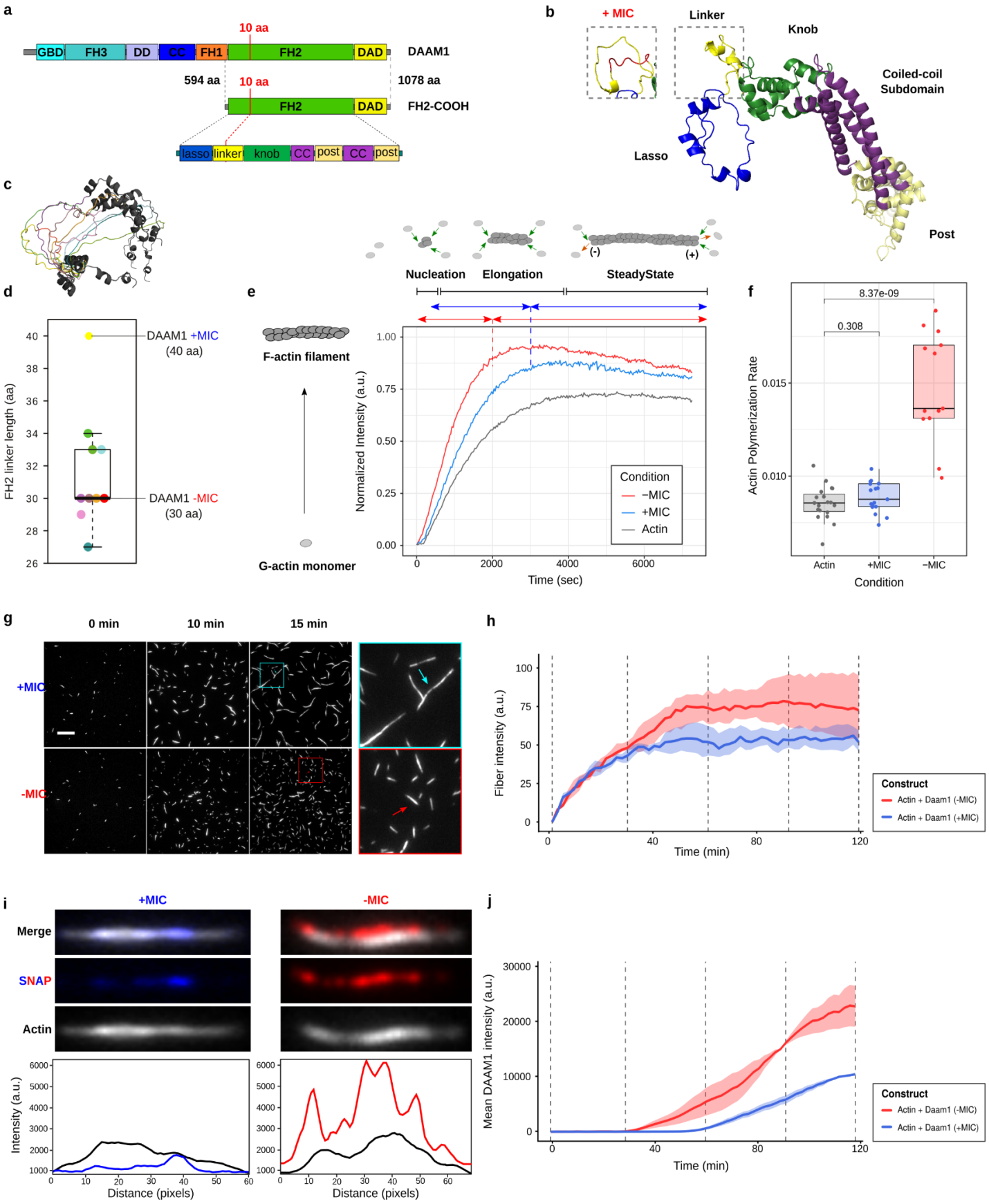
a
10 aa
GBD
FH3
DD
CC
FH1
FH2
DAD
DAAM1
594 aa
10 aa
1078 aa
FH2
DAD
FH2-COOH
lasso
linker
knob
CC
post
CC
post
b
+ MIC
Linker
Knob
Coiled-coil Subdomain
Lasso
Post
c
Nucleation
Elongation
SteadyState
(-)
(+)
d
FH2 linker length (aa)
DAAM1 +MIC (40 aa)
DAAM1 -MIC (30 aa)
e
F-actin filament
G-actin monomer
Normalized Intensity (a.u.)
Time (sec)
Condition
−MIC
+MIC
Actin
f
8.37e-09
0.308
Actin Polymerization Rate
Actin
+MIC
−MIC
Condition
g
0 min
10 min
15 min
+MIC
-MIC
h
Fiber intensity (a.u.)
Time (min)
Construct
Actin + Daam1 (-MIC)
Actin + Daam1 (+MIC)
i
+MIC
-MIC
Merge
SNAP
Actin
Intensity (a.u.)
Distance (pixels)
j
Mean DAAM1 intensity (a.u.)
Time (min)
Construct
Actin + Daam1 (-MIC)
Actin + Daam1 (+MIC)

Figure 2 - Splice variants of the DAAM1 FH2-COOH fragment differentially modulate actin dynamics. (a) Schematic representation of DAAM1 domains (top) and subdivisions within the FH2 domain (bottom). FH2-COOH corresponds to the purified protein fragment. Domain nomenclature as in Figure 1e. (b) Structure of the FH2 domain with (left) or without (right) microexon inclusion. Subregions of the lasso, linker, coiled-coil as well as knob and post regions share the same color-code as in (a). (c) Structural comparison of the FH2 linker regions among all human formin proteins. Structures taken from AlphaFold2 and visualized using the program PyMoL. (d) Lengths of the FH2 linker regions across formin proteins. Linker color corresponds to the structures in (c). (e) Pyrene actin polymerization assay. Each curve is the average of five technical replicates. Schematic representations of the nucleation, elongation, and steady-state phases of actin polymerization from the "Actin" profile are represented above. (f) Actin polymerization rates from four independent experiments. Rates correspond to the slope of the curves at 50% assembly (Doolittle, Rosen, and Padrick 2013). Data points correspond to values from all technical replicates from four independent experiments. P-values from Wilcoxon rank-sum tests. (g) Representative images from time series of fluorescence micrographs showing F-actin fibers stained with SiR-Actin in presence of microexon containing (+MIC) or non-containing (-MIC) splice variant of the FH2-COOH fragment of human DAAM1. 2 µM Actin and 200nM DAAM1 fragments were used. Scale bar: 10 µm. On the right, zoom-in of the regions of interest depicted in the 15 min time point. Arrows indicate differences in actin fiber morphology. (h) Quantification of total fiber intensity through the course of the experiments performed using 0.2 µM actin and 200 nM DAAM1 fragments. Thick lines represent the median from four independent experimental replicates, and the dispersion corresponds to the first and third quartiles. Statistical tests can be found in Figure S2i. (i) Dual-color TIRF microscopy of actin fibers obtained after 50 min using 0.2 µM actin and 200 nM SNAP-tagged proteins. The upper panel shows representative images of the actin fibers considered for the analysis while the lower panel displays the fluorescence intensity distribution along the fibers obtained using the line profile function of Fiji (black indicates actin, and red and blue the +MIC and -MIC proteins, respectively). (j) Quantification of protein fluorescence intensity along actin fibers as a function of time using 0.2 µM actin and 200 nM SNAP-tagged proteins. Thick lines represent the median from two independent experimental replicates, and the dispersion corresponds to the first and the third quartiles. Statistical tests for selected time points can be found in Figure S3f.

morphology. However, we observed a mild, but statistically significant, increase in neurite length (Figure 3c), together with a slight increase in filopodia length (Figure 3d), but no major changes in filopodia number (Figure S4c). Immunostaining of DAAM1, actin and α-tubulin showed no major changes in the protein signal within the growth cones (Figure S4d,e), with only a small but significant relative reduction of DAAM1 and actin in more distal filopodia (Figure S4f,g).

Despite these mild effects on neuritogenesis, microexon deletion did not impair the ability of neurons to fully differentiate, as both WT and KO cell lines successfully generated neuronal networks. Furthermore, calcium imaging showed no major differences in basal calcium influx between WT and KO cell lines throughout differentiation (Figure S4h), nor upon neuronal depolarization with KCl at early and mid differentiation stages (DIV1 and DIV7) (Figure 3f). However, mature KO neurons (DIV14 and DIV21), which formed synaptic connections, exhibited a strong and significant increase in Ca2+ influx upon depolarization (Figure 3e,f). Thus, we next focused on mature neuronal cultures, where we performed chemical treatments with modulators of various aspects of actin dynamics (Figure 3g). Reduction of F-actin polymerization accomplished by sequestering available G-actin monomers with Latrunculin A (LatA) resulted in a strong reduction of calcium influx in both WT and KO cell lines (Figure 3g,h). Importantly, in contrast to control treatments, no major differences were observed between the two genotypes (Figure 3g,h), suggesting that the genotype differences in calcium influx are largely dependent on actin polymerization dynamics. Next, we applied SMIFH2, a small molecular inhibitor of formin FH2 domains that selectively inhibits formin-driven actin polymerization without impairing the function of other ABPs. We found that exposure of neuronal cultures to SMIFH2 increased Ca2+ influx in WT cell lines, mimicking the KO phenotype (Figure 3g,h). This suggests that microexon removal in neurons may lead to impaired activity of the FH2 domain of DAAM1, at least in relation to Ca2+ influx upon depolarization. Finally, the increase in Ca2+ influx observed in Daam1-MIC KO neurons was not due to differences in DAAM1 isoform localization to the synapses, since DAAM1 similarly co-localized with the synaptic marker Syp-1 in both WT and KO cells (Figure S4i), nor to changes in protein expression since only a small and non-significant decrease in neuronal DAAM1 protein levels was observed upon MIC deletion (Figure S4j).

Daam1-MIC KO mice exhibit neuronal postnatal defects

We next generated a mouse KO line for Daam1-MIC by blastocyst microinjection of one of the CRISPR-Cas9 edited ESC lines (see Methods). RT-PCR assays confirmed the successful microexon deletion in mice (Figure S5a). In contrast to the full gene KO (Nakaya et al. 2020), Daam1-MIC KO was not lethal, and mutant mice were born with expected Mendelian ratios (Figure S5b), had normal weight (Figure S5c) and did not display gross morphological abnormalities. To assess putative effects on motor development and/or psychomotor impairments during the pre-weaning period, we first performed a neurodevelopmental behavioral screen (Figure 4a) (Feather-Schussler and Ferguson 2016; Roper et al. 2020). Mutant mice showed no differences in surface righting (Figure S5d), grasping reflex (Figure S5e), cliff aversion (Figure S5f) and Prayer´s reflex (Figure S5g), in comparison to the WT. Moreover, the negative geotaxis test, which allows the simultaneous assessment of vestibular function, paw strength and motor coordination (Ruhela et al. 2019; Feather-Schussler and Ferguson 2016; Roper et al. 2020) did not reveal significant differences between WT and mutant mice throughout development (Figure S5h,i). However, the forelimb and hindlimb strength of mutant pups were increased compared to WT siblings (Figure 4b,c). In the forelimb suspension test, heterozygous mice showed a significant increase in suspension time at postnatal day 10 (PD10) ($P = 0.009$, Wilcoxon rank-sum test), with homozygous KO mice displaying the same trend but not reaching statistical significance ($P = 0.335$, Wilcoxon rank-sum test). Hindlimb suspension was significantly better in KO mice at PD10, when the majority of homozygous and heterozygous mutants scored the maximum hanging score and showed higher hindlimb separation (Figure 4c; PD10 homozygous: $P = 0.007$, Wilcoxon rank-sum test). Additionally, motor development-dependent walking, which results from increased neuromotor strengthening and an increase in limb coordination (Roper et al. 2020), also exhibited significant differences (Figure 4d), with homozygous KO mice walking significantly earlier ($P = 0.010$, PD7, Wilcoxon rank-sum test). However, at PD10, a significant increase of walking latency was detected in both mutant phenotypes in comparison to the WT (PD10: heterozygous $P = 0.008$, homozygous $P = 0.001$, Wilcoxon rank-sum test). Interestingly, the homing task, which analyzes general psychomotor development, also revealed a significant delay in finding the nesting material in mutant mice (Figure 4e; heterozygous $P = 0.032$, homozygous $P = 0.018$, Wilcoxon rank-sum test). In summary, while motor development seems slightly better, mutant pups show slower development of social cognitive abilities.

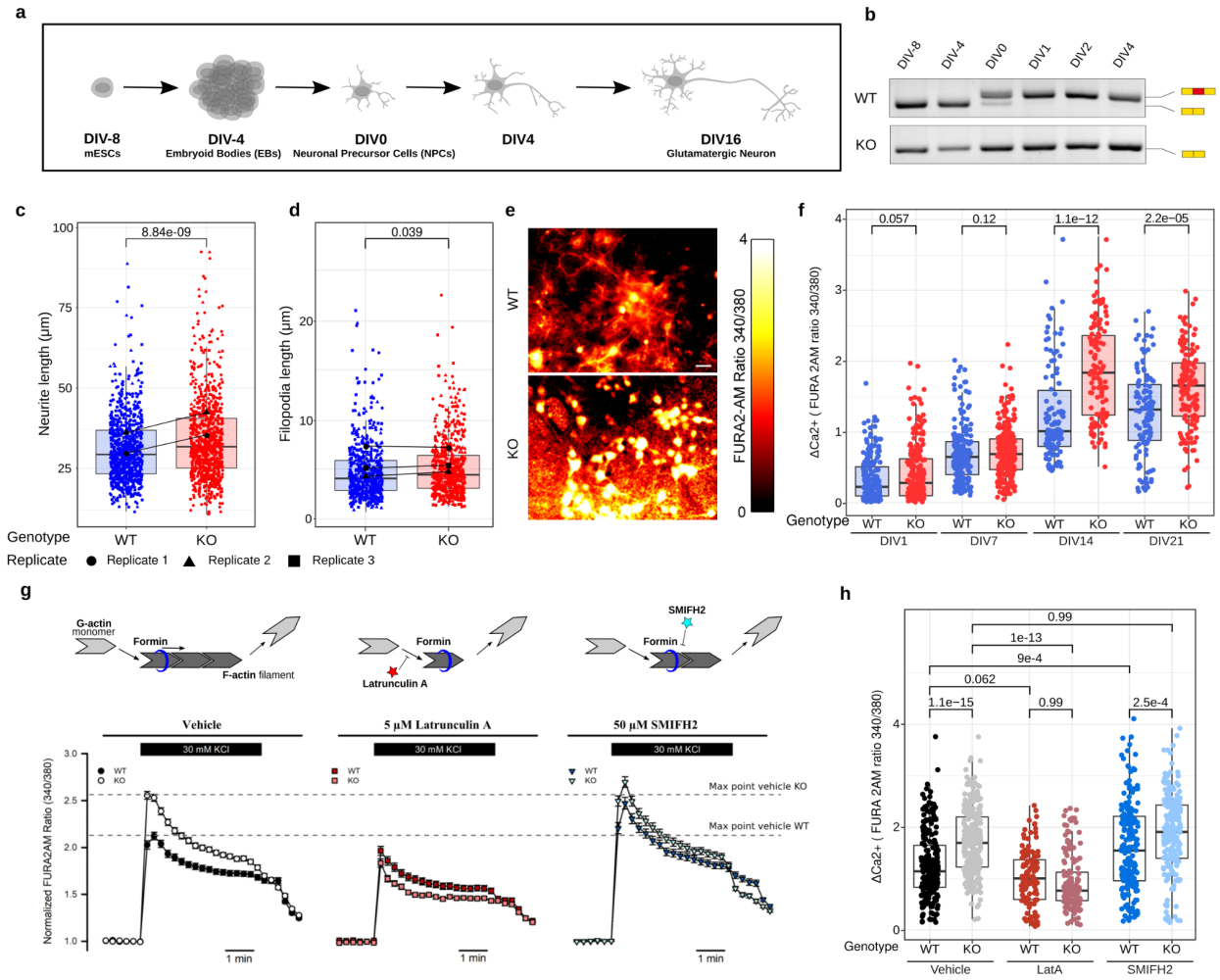

Figure 3 - Daam1-MIC removal increases calcium flux in glutamatergic neurons. (a) Schematic representation of the neuronal differentiation protocol. DIV - day in vitro. (b) RT-PCR assays of Daam1-MIC inclusion during neuronal differentiation in representative WT and KO cell lines. (c,d) Distributions of the lengths of the longest neurites (c) and of individual filopodia (d) of neuronal precursors (DIV0+4h). P-values from two-way ANOVA tests with replicate and genotype as factors. (e) Representative images of the calcium imaging experiment performed using FURA-2AM in mature neuronal cells (DIV21) depolarised with 30 mM KCl isotonic solution. Scale bar: 10 µm. (f) Distributions of calcium influx in WT and KO cell lines at various differentiation time points, based on FURA 2AM ratio.Neurons were stimulated with a 30 mM KCl isotonic solution. P-values from Wilcoxon rank sum tests. (g) Effects of the actin polymerization inhibitor Latrunculin A (LatA) and the small molecular inhibitor of formin FH2 domains (SMIFH2) on calcium currents in differentiated glutamatergic neurons at DIV14-21. Data corresponds to three independent experiments. Top: schematic representation of the mode of action of the actin modulating drugs. (h) Distributions of calcium influx in WT and KO cell lines upon different treatments as depicted in (g), based on FURA 2AM ratio. P-values from Wilcoxon rank sum tests.

We next investigated potential cellular abnormalities associated with these postnatal developmental phenotypes. No gross anatomical differences were found in the hippocampus of KO compared to control mice (Figure S5l). Moreover, we found no major defects in neuronal branching as measured by the distance between the cell body and first dendritic branch (Figure S5m,n). However, the subcellular analysis of pre- (Synapsin 1/2) and post- (PSD95) synaptic markers showed striking differences between genotypes in the matching of these two proteins (Figure 4f,g). While no changes were observed in the number of presynapses in the CA1 region of the hippocampus, we observed a significant decrease in PSD95-positive excitatory synapses, suggesting a severe impairment of the postsynaptic densities in KO mice (Figure S5o,p). Furthermore, we observed increased levels of Activity Regulated Cytoskeleton Associated Protein (ARC) in the dentate gyrus (Figure 4h,i), with a significantly higher density of ARC positive nuclei in KO compared to WT mice. Thus, altogether, these results suggest potential defects in post-synaptic formation and function.

Daam1-MIC deletion results in learning and memory deficits in adult mice

We next assessed a range of potential defects in adult mice, including motor, behavioral and learning phenotypes. No significant differences in forelimb grip strength were observed (Figure 5a), with KO males showing only a mild trend for increased strength. Consistently, the rotating rod test (Rotarod) showed no significant differences in the training, coordination (constant speed) or acceleration sessions (Figure S6a-c). The lack of major changes in motor function was further

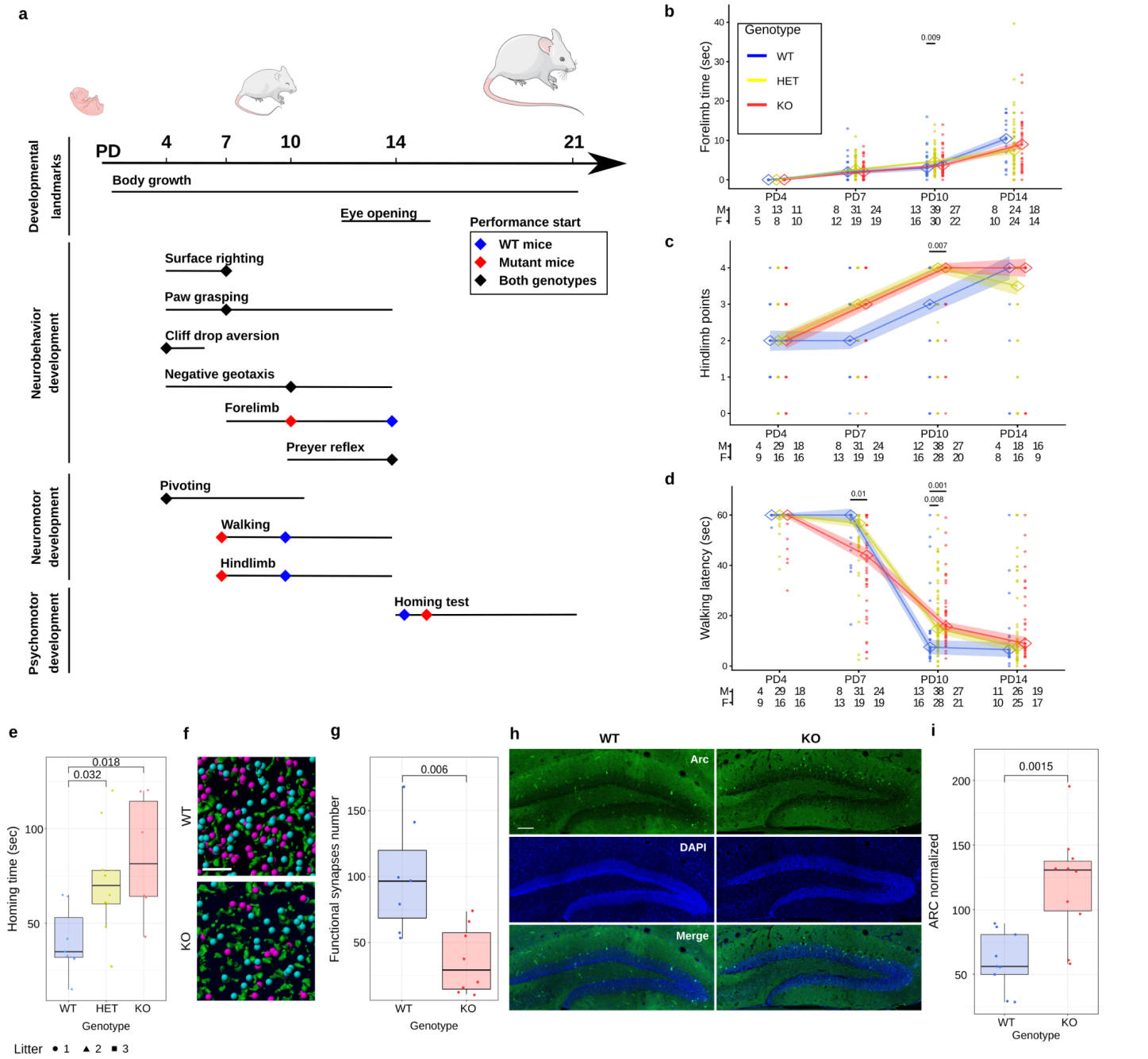

Figure 4 - Early postnatal development effects of Daam1-MIC deletion. (a) Mouse postnatal developmental timeline and summary of the results of the neurodevelopmental experiments performed on days 4, 7, 10, 14, and 21. Lines represent the span between the start and the end of each experiment, while diamonds indicate when >50% of animals of a given genotype achieve a specific level of performance. Blue and red diamonds correspond to WT and mutant mice, respectively, whereas black diamonds indicate similar performance. PD - postnatal days. Mouse icons derived from bioicons.com. (b-d) Animal performance at each indicated time point for forelimb strength (b), hindlimb separation score (c), and latency to walk (d). Thick lines represent mean performance, shading represents the standard error mean (SEM). Dots represent values measured per animal. Number of animals per time point, genotype (WT, heterozygous [HET] and homozygous [KO] mutant) and sex (males [M] and females [F]) are shown at the bottom. P-values from Wilcoxon rank-sum tests against the corresponding WT. (e) Distributions of times needed to perform the homing test per genotype. Values for matched litters are indicated with symbols. P-values from Wilcoxon rank-sum tests. (f) 3D reconstructions of pre- (Synapsin1/2, green) and post- (PSD95, blue and pink) synaptic markers in PD22 CA1 hippocampal sections. Pink spots represent postsynapses at ≤0.5µm from the presynapses (functional synapses) and blue ones those at >0.5µm. (g) Distributions of the percentage of functional synapses normalized to the control mean for WT and KO animals. P-values from Wilcoxon rank sum tests. (h) Representative images of ARC immunohistochemistry (green) and DAPI stained nuclei (blue) in sections of the dentate gyrus of the hippocampus from PD21 mice (PD21). (i) Quantifications of ARC-positive nuclei in hippocampal dentate gyrus across images normalized to the dentate gyrus size (Figure S5l). One dot represents one animal, for which an average of 3-6 coronal views of the hippocampus were analyzed. P-values from two-way ANOVA tests with replicate and genotype as factors.

confirmed by the beam balance test, where no significant point-based score differences were found, and the majority of animals reached the escape route irrespective of their genotype (Figure S6d). Of note, female KO mice displayed an increased number of slips during the tests (Figure S6e).

Next, we evaluated anxiety-related phenotypes. In the elevated plus maze test (Figure 5b) (Walf and Frye 2007), no major changes in the relative time spent in the open arms were observed between the genotypes (Figure 5c). However, analyses of additional parameters pointed at a potentially mild anxiety-like behavior only in females, including increased latency to first entering the center of the maze (Figure S6f). Additionally, we used an actimeter to quantify spontaneous locomotor activity for 23h, spanning a day-night cycle. No significant changes were seen in general behavior (Figure S6g), but a trend towards higher activity during the night in KO animals was observed (Figure S6g,h).

We then investigated learning and memory formation capabilities upon Daam1-MIC removal. First, to evaluate recognition memory, we used the novel object recognition (NOR) task (Figure 5d), which depends on the prefrontal cortex and hippocampal circuit responsible for cognitive processing (Leger et al. 2013; Warburton and Brown 2015; Lueptow 2017). No significant differences in total exploration time were observed during the familiarization or test phases of the experiment (Figure S7a,b). Remarkably, KO mice of both sexes showed significantly impaired recognition memory, as assessed by the discrimination index (Figure 5e). Second, we evaluated spatial memory by employing a modification of the Morris Water Maze (MWM) task (Figures 5f,g and see Methods)(Vorhees and Williams 2006). As expected, both KO and WT mice showed a progressive reduction in the escape latency time (Figures S7e). However, spatial learning was impaired in KO males in comparison to WT males between days 4 and 8 (Figures 5h,i and S7e,f). This impairment was not due to motor or motivation defects, as no impairment was detected during the cued session when the platform is visible (Figure 5h,i). In stark contrast, no significant differences were found in KO females (Figure 5h,i and S7e,f). Finally, the contextual fear conditioning test did not show differences in freezing in male KO compared to WT mice (Figure S7g,h). Interestingly, analysis of immediate early genes in dentate gyrus performed 1.5 h after this test showed clear downregulation of cFOS but not ARC protein positive nuclei in KO mice (Figure S7i,j). No differences on cFOS positive cells were observed in basal conditions (Figure S5l-o). Importantly, Western Blot analysis did not show differences in DAAM1 protein expression levels in mouse cerebellum, motor cortex, or other tissues (Figure S7p-r). Altogether, these results suggest that Daam1-MIC removal negatively impacts memory formation in adult mice, which cannot be attributed to impaired motor function or to anxiety-related behaviors.

Daam1-MIC deletion impacts long-term potentiation

Our results thus far showed that microexon deletion leads to increased neuronal calcium influx in vitro, and hippocampal-dependent learning and memory defects in vivo. To obtain further mechanistic insights into these phenotypes, we next investigated how Daam1-MIC deletion affected synaptic function and plasticity in hippocampal slices from WT and KO adult males. Whole-cell voltage-clamp recording in CA1 pyramidal cells of the hippocampus showed a trend for a higher number of spikes in response to suprathreshold depolarizing current (Figure S8a), suggesting a mild increase in the firing rate compared to WT neurons (Figure S8b), which did not reach statistical significance. We also did not observe significant changes in the set of parameters that describe intrinsic membrane properties (rheobase, membrane resistance, membrane potential and threshold action potential; Figure S8c-h), indicating that ionic permeability was not affected, and there were no major changes in membrane conductance in KO cells.

We next studied the effect of Daam1-MIC deletion on glutamatergic CA3-CA1 synapses from hippocampal brain slices of adult mice. We induced Long-Term Potentiation (LTP) using a theta burst stimulation (TBS). The results showed a strong and significant decrease in field excitatory postsynaptic potential (fEPSP) response in KO compared to WT neurons (Figure 6a,b). To explore possible mechanisms behind this phenotype, we then examined basal synaptic transmission in the CA1 region (input-output relationship of excitatory postsynaptic currents (EPSC)) and the presynaptic release of neurotransmitter, by applying paired-pulse facilitation protocol (PPF) and recording miniature EPSCs (mEPSCs). These analyses did not show significant differences between WT and KO mice (Figures S8i-n), suggesting no changes in basal excitatory synaptic transmission at hippocampal (CA3-CA1 neuron) synapses upon Daam1-MIC deletion, and ruling out major presynaptic changes associated with the LTP deficit in KO slices. In contrast, and consistent with the specific reduction of the postsynaptic densities at PD22 (Figures 4f and S5o,p), biocytin labeling on patch-clamped neurons (Figure 6c) revealed a trend towards a reduced number of dendritic spines (Figure 6c,d), reaching statistical significance specifically for thin immature spines in KO neurons (Figure 6e). No significant changes were observed for stubby and mushroom-like spines (Figures S8o).

Taken together, these results suggest that Daam1-MIC deletion alters molecular pathways essential for proper formation of dendritic spines and LTP. Therefore, to investigate possible molecular phenotypes associated with these defects, we performed RNA-seq analysis of five male hippocampi from WT and KO mice used in behavior experiments, which showed only mild, non-significant changes in the expression of individual genes. However, Gene Set Variation Analysis (GSVA)(Hänzelmann, Castelo, and Guinney 2013) revealed significant mis-regulation of several pre- and postsynaptic pathways (Figures S9a). For instance, multiple genes involved in the "synaptic vesicle cycle" (KEGG mmu04721) were found to be downregulated in KO compared to WT samples (Figures S9b-d). Furthermore, the level of expression of synaptic vesicle cycle pathway genes in each mouse hippocampus was significantly positively correlated with their individual performance in the NOR task (Figures S9e). This includes some essential genes in synaptic vesicle cycling such as Unc13, Unc18, RIMs, VAMPs, Syntaxins, and Rab3a (Figures S9f). In addition, GSVA also revealed mis-regulation of multiple post-synaptic genes, as exemplified with the cholinergic (which also participates directly in memory and learning by sending information to the hippocampus) and dopaminergic (which regulates behavior and reward) synapse pathways (KEGG mmu04725 and mmu04728; Figures S10a-e).

Since these changes in gene expression upon DAAM1-MIC KO were mild overall, we next focused on other molecular players important for dendritic spine morphology. As DAAM1 has been shown to interact with RhoA causing its activation (Habas, Kato, and He 2001; Higashi et al. 2008; Kühn and Geyer KO2014) and RhoA activity is important to regulate both LTP and dendritic spine formation (Haorui Zhang et al. 2021), we determined RhoA activity with a FRET-based biosensor (Fritz et al. 2013) using in vitro differentiated mature neuronal cultures. FRET efficiency measured by acceptor photobleaching revealed a robust and significant increase in RhoA activity in protrusions of KO compared to WT neurons (Figures 6f,g and S10f).

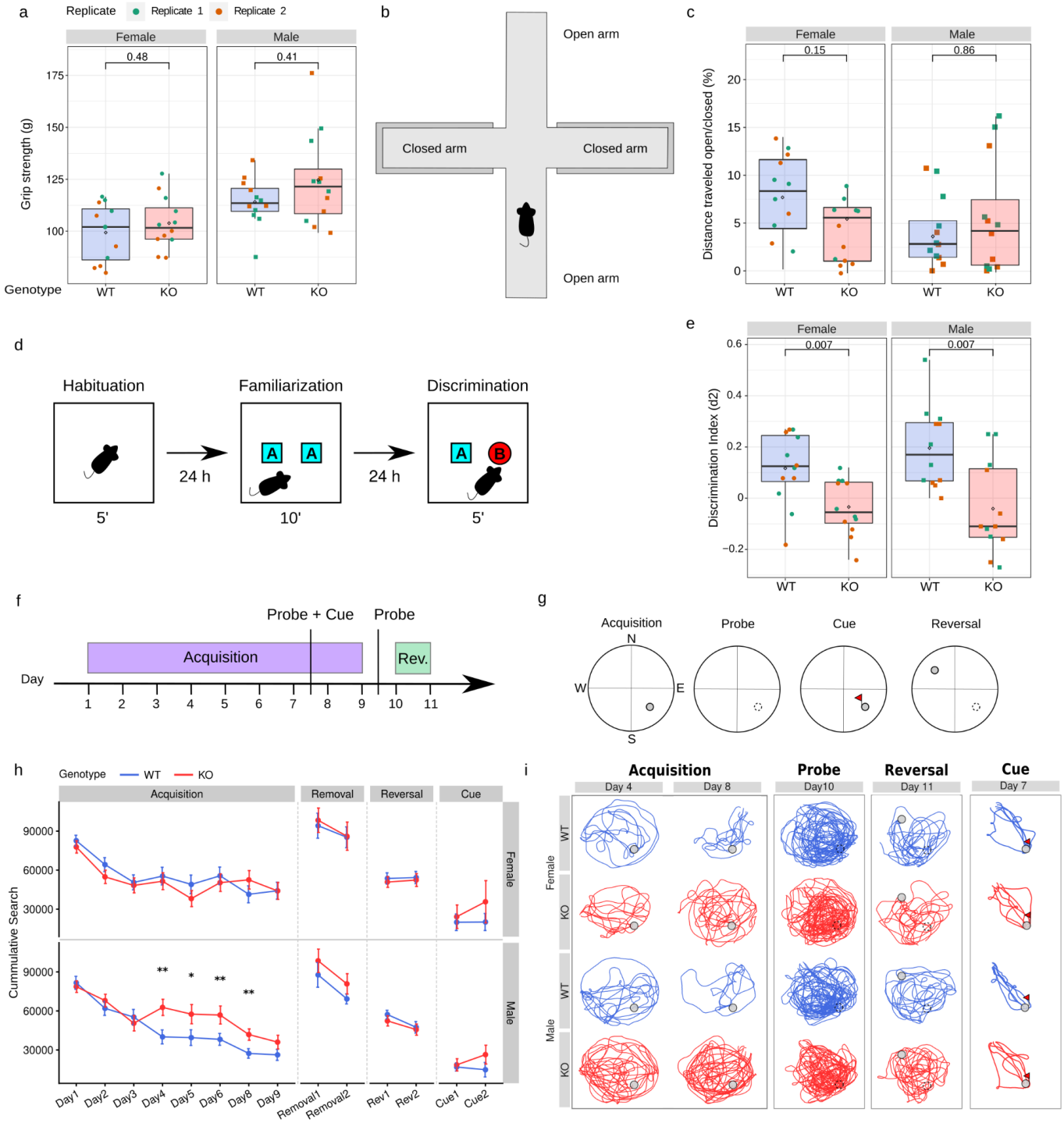

Figure 5 - Daam1-MIC removal causes recognition and spatial learning impairments in adult mice. (a) Distributions of maximal peak force developed as a measure of forelimb grip strength in adults. Each value corresponds to the average of three replicate measures per mouse. (b) Schematic representation of the elevated plus maze experiment. Red rectangles describe the open arm ends. (c) Distributions of the ratio of the time spent in the open vs. closed arms of the plus maze. P-values from Wilcoxon rank sum tests. (d) Schematic representation of the Novel Object Recognition (NOR) experiment. The experiment consists of three sessions: habituation, familiarization and discrimination (length of 5 min, 10 min, and 5 min, respectively). Each session was separated by 24 h periods. (e) Distribution of discrimination index (d2) values quantified during the NOR discrimination phase. The discrimination index corresponds to: (Novel Object Exploration Time - Familiar Object Exploration Time)/ Total Exploration Time. For panels (a,c,e), one dot describes the performance of one animal. P-values from Wilcoxon rank-sum tests. (f,g) Schematic representation of the Morris Water Maze protocol (f) and platform set-ups (g) (details in Supplementary Methods). (h) Cumulative search index during the acquisition, removal, reversal and cued phases for females (top) and males (bottom) based on (Tomás Pereira and Burwell 2015). Distributions of values for days 4 and 8 are shown in Figure S7f. P-values from two-way ANOVA tests with replicate and genotype as factors. (i) Representative combined trajectories of performances of all six animals from one trial of experimental replicate 1 during each phase of the Morris Water Maze.

Lastly, immunocytochemistry assays in neuronal cultures also revealed consistently higher basal levels of ARC in KO compared to WT cells, in line with the results from P21 mice hippocampal slices in basal conditions Figure 4g,h), whereas no changes for cFOS or EGR1 immediate early genes were observed (Figure 6h,i and S10g). Altogether, these results point towards profound alterations in two key molecular components, RhoA and ARC, which are known to interact with DAAM1 and the actin cytoskeleton, respectively.

Discussion

Tight regulation of the actin cytoskeleton by ABPs is crucial for multiple neurobiological processes, from neurogenesis to higher functions of adult brains, such as memory and learning. Here, we found that Daam1, the formin gene with the highest expression in mature neurons, harbors a microexon that is highly neural-specific and evolutionarily conserved across vertebrates. Inclusion of this microexon extends the length of the linker region of the FH2 domain, modulating its actin polymerization capabilities, both quantitatively and qualitatively, in controlled in vitro assays. Deletion of Daam1-MIC in neurons led to a unique pattern of physiological alterations, among them increased calcium influx, while mice without this microexon exhibited diverse phenotypes, including a decreased number of dendritic spines, defects in memory formation and reduced LTP.

Neuronal microexon inclusion makes DAAM1's FH2 linker region an outlier with respect to the length of all other formins. Given that the linker region serves as a hinge in FH2 dimers(Schönichen and Geyer 2010), its uniquely large length likely results in a much more flexible dimer, which we show to bind less to actin filaments compared to the skipping, non-neural isoform. Previous studies(Yamashita et al. 2007; Moseley, Maiti, and Goode 2006) reported that the long linker of DAAM1 was associated with the unusually low actin polymerization rate of this protein, and that its artificial shortening enhanced polymerization. Whereas we recapitulate these quantitative findings, our TIRF results revealed a much more complex scenario in which the microexon inclusion does not simply lead to a reduced polymerization rate but also to a dramatic change in how DAAM1 interacts with and remodels the actin cytoskeleton. In particular, we observed that microexon removal significantly increased the actin-bundling capabilities of DAAM1, probably as a direct result of a higher affinity to actin. Moreover, a detailed structural characterization of these actin bundles showed that the microexon-containing isoform produced consistently longer and more branched fibers, likely due to its less constrained binding to actin. Although these results are based on in vitro assembly assays, it is tempting to speculate that, in vivo, the inclusion or exclusion of the microexon may similarly modulate DAAM1's behavior with actin and hence its function.

Why is a different mode of action of DAAM1 favored in neurons versus other cell types? How does microexon removal impact DAAM1's function in neurons, resulting in decreased dendritic spine number, impaired LTP and memory formation? Based on our observations, we propose that the inclusion of Daam1-MIC is preferred because of its impact on actin dynamicity and turnover, which is crucial for the complex morphology of dendritic spines and the functionality of synaptic terminals. Given that the formation, maturation and plasticity of spines are all highly dependent on the actin cytoskeleton remodeling (Haorui Zhang et al. 2021), it seems plausible that splicing-dependent modulation of DAAM1's mode of action increases its versatility and hence actin dynamics. In this scenario, less dynamic actin networks caused by increased bundling of actin filaments upon microexon removal, as observed in vitro, could be detrimental during LTP consolidation by delaying or even blocking efficient rearrangement of the actin cytoskeleton during the learning process. Moreover, microexon deletion in KO neurons could lead to the formation of a distinct submembranous actin cortex that alters the shape and receptor composition of postsynaptic terminals and thus neurotransmitter receiving.

In this study, we decided to perform a multi-level characterization of the phenotypes observed upon Daam1-MIC deletion, while future work should focus on elucidating the specific mechanisms connecting Daam1-MIC deletion and deregulation of actin dynamics with the observed cellular and organismal phenotypes. However, two molecular phenotypes that we observed in Daam1-MIC KO neurons, increased RhoA activity and mis-regulation of basal ARC protein levels, provide initial insights into the underlying mechanisms of impaired memory formation. Our results showed a lower number of thin dendritic spines upon Daam1-MIC removal. These thin, immature spines are characterized by their dynamic structure and can be considered "learning spines", as they can be consolidated into more stable mushroom spines (Haorui Zhang et al. 2021). Rho-family GTPases, including RhoA, are key players in the process of memory formation by regulating spine morphology. Growing evidence suggests that RhoA activity modulates immature spine pruning (Bolognin et al. 2014; Haorui Zhang et al. 2021). For instance, expression of constitutively active RhoA in hippocampal neuronal cultures or brain slices resulted in simplified dendritic trees and reduced spine densities (Nakayama, Harms, and Luo 2000; Impey et al. 2010). Conversely, RhoA inhibition specifically increases the number of immature spines (Nakayama, Harms, and Luo 2000). These findings are consistent with both the increased RhoA activity we observed in cultures upon Daam1-MIC removal, and the decreased number of PSD95-positive postsynaptic densities and of thin spines in hippocampal slices of KO mice. How does Daam1-MIC removal lead to increased RhoA activity? Interestingly, DAAM1 interacts with RhoA through its amino-terminal GDB domain, causing its activation(Kühn and Geyer 2014; Higashi et al. 2008; Habas, Kato, and He 2001). Even though the microexon does not lie in the proximity of the GDB domain, and previous studies did not show significant changes in direct DAAM1-RhoA interaction upon microexon inclusion or exclusion (Ellis et al. 2012), it is possible that changes in unbound DAAM1 availability, local protein concentration and/or turnover impact DAAM1-mediated RhoA activation. Alternatively, higher RhoA activation could be indirectly due to changes in actin turnover caused by the deletion of Daam1-MIC.

Additionally, the immediate early gene Arc is known to regulate actin cytoskeleton and to control spine morphology during the LTP and long-term depression (LTD) processes (Hongyu Zhang and Bramham 2021). Importantly, the translation of ARC is regulated locally in dendritic spines (Newpher et al. 2018), and newly synthesized ARC impacts actin dynamics by interaction with many ABPs and other actin regulating proteins (e.g. cofilin, CaMKIIβ and drebrin A) (Okuno et al. 2012; Messaoudi et al. 2007; Nakahata and Yasuda 2018). Moreover, during Arc-dependent LTP consolidation, local ARC protein translation is dependent on actin polymerization (Huang, Chotiner, and Steward 2007). Our data consistently showed increased ARC protein levels in basal conditions upon Daam1-MIC removal, with no significant changes at the mRNA level. Thus, it is plausible that enhanced actin bundling upon microexon removal creates the platform for more efficient Arc mRNA docking in dendritic spines and hence higher ARC translation in basal conditions. Interestingly, newly synthesized ARC

accumulates in non-stimulated spines and suppresses synaptic potentiation by decreasing the amounts of AMPA receptors in the postsynaptic surface (Okuno et al. 2012, Newpher et al. 2018), in line with a role for ARC expression in inhibiting LTP (Plath et al. 2006; Rial Verde et al. 2006). Remarkably, RhoA also plays a role in the regulation of AMPA receptor trafficking, where activation of RhoA is associated with decreased surface AMPA receptors (Shen et al. 2020). Altogether, these data suggest numerous molecular interplays between RhoA, ARC and the actin cytoskeleton that could determine the fate of dendritic spines and have an effect on LTP. However, the exact role of DAAM1 as a central player regulating these interplays still needs to be investigated in detail.

In summary, through a comparative analysis of formin proteins, we found that Daam1 is subject to tight post-transcriptional regulation by a highly neural-specific and evolutionarily conserved microexon that impacts actin polymerization via modulation of its FH2 domain. Moreover, through an in-depth multi-level characterization of this microexon, we unveiled DAAM1 as a new key player for the regulation of neurotransmission and memory formation.

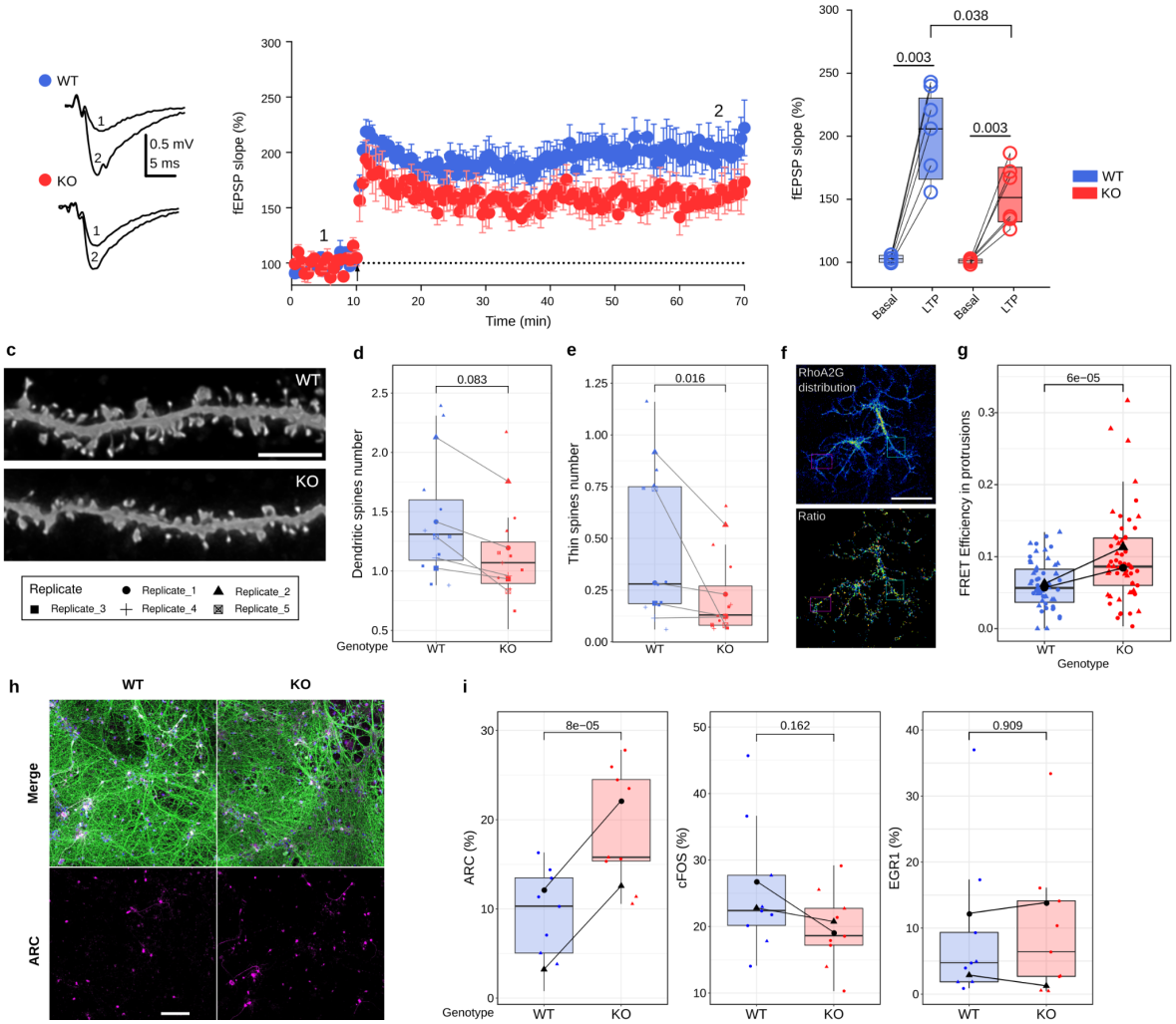

Figure 6 - Loss of Daam1-MIC impairs hippocampal long-term potentiation (LTP). (a) Field excitatory postsynaptic potentials (fEPSPs) were recorded in the CA1 dendritic layer in response to CA1 Schaffer collateral stimulation. LTP was induced by theta burst stimulation (TBS; 10 bursts of 5 pulses at 100 Hz, with an interval of 200 ms between bursts). LTP temporal plot of fEPSP values in KO (red circles, n= 6, N= 5) compared to WT mice (blue circles, n = 5, N = 3) after TBS at 60 min. Insets of traces in the plots represent average fEPSPs recorded during periods indicated by corresponding numbers in the graph (1 and 2). (b) Boxplot of LTP after TBS at 60 min. P-values from Welch's t-tests (p= 0.038, t= 2.538 with 7.183 degrees of freedom). (c) Representative maximum-intensity confocal images of dye-filled dendrites and dendritic spines after deconvolution. Scale bars: 5 µm. (d,e) Number of total dendritic spines (d) and of thin spines (e). N = 5 mice for each genotype, 100 µm of dendrites per cell. One dot represents one neuron analyzed. Lines represent the relation between animals analyzed in experimental replicates. P-values from Wilcoxon rank-sum tests. (f) Confocal micrographs representing RhoA2G distribution (top) and RhoA activity (sensor ratio; bottom) in mature neuronal cells (DIV21). Scale bar: 50 µm. (g) Comparison of the RhoA2G biosensor FRET efficiency between WT and KO cell lines using fluorescent microscopy. One dot represents FRET efficiency in one neuron. P-values from two-way ANOVA tests with replicate and genotype as factors. (h) Representative images of immunocytochemical assays of ARC-positive nuclei in glutamatergic neurons (DIV21). Merge corresponds to ARC (magenta), β3-Tubulin (green) and DAPI (blue) staining overlap. Scale bar: 100 µm. (i) Number of ARC, FOS and EGR1 positive neuronal nuclei normalized to the total nuclei number based on DAPI. Dots correspond to the average values of three independent ROIs measured on individual cell lines. P-values from two-way ANOVA tests with replicate and genotype as factors.

Materials and Methods

Computational analysis formins and characterization of DAAM1 and RT-PCR assays

To investigate the expression of formins across tissues and during neuronal differentiation (Fig. 1a), we used mouse (mm10) data from VastDB (Tapial et al. 2017). In addition, we extracted the mouse and/or human neural-regulated exons among the 15 mammalian formin genes from Table S2 in (Irimia et al. 2014) and used VastDB to extract the exon's protein location and inclusion levels for the six identified neural regulated exons shown in Fig 1b and 1c, respectively. The study of the evolutionary conservation of these six exons was carried out using the VastDB ortholog information and manual exon alignments among the human (hg38), mouse (mm10), cow (bosTau9), opossum (monDom5), chicken (galGal4), frog (xenTro9), zebrafish (danRer10) and shark (calMil1) genomes, downloaded from Ensembl. To investigate the regulation of Daam1-MIC by SRRM3/4 (Fig. 1i), we used data from human HEK293 cells overexpressing human SRRM4 (GEO: GSE112600 (Torres-Méndez et al. 2019)), mouse N2A cells upon Srrm3/4 knockdown (SRA: PRJNA47491 (Gonatopoulos-Pournatzis et al. 2018)), and zebrafish retinae extracted from Srrm3 KO 5 days post fertilization larvae (GEO: GSE180781 (Ciampi et al. 2022)). Crystal Structure of human DAAM1 FH2 domain (2z6e.pdb) was used to model the mice Daam1 FH2 domain with and without microexon using Robetta (http://new.robetta.org/) (Fig. 2b). Visualization was performed using the PyMoL program.

To validate the inclusion of Daam1-MIC through RT-PCR assays in mouse and zebrafish (Fig. 1h and throughout the manuscript), total RNA was extracted using the RNeasy Plus Mini kit (Qiagen, 74136), treated with DNase using TURBO DNA-freeTM Kit (Thermo Fisher Scientific), and reverse-transcribed with SuperScript III Reverse transcriptase (Invitrogen, 18080044) and oligo(dT)20 as advised by the manufacturer. GoTaq G2 Flexi DNA Polymerase enzyme (Promega, M7806) was used to amplify Daam1-MIC's flanking exons and PCR assays were performed with 25 cycles, 54°C annealing temperature and 120 sec extension. The PCR product was size-fractionated using 2.5% ultrapure agarose (Invitrogen, 16500500) in SB buffer (36.4 mM of Boric acid and 10 mM NaOH), and detected using SYBR Safe (Life Technologies, S33102). Primer sequences used in this study are provided in Table S1.

Cloning of Daam1 FH2 domain, protein expression and purification

To clone the functional FH2 domain of DAAM1 (residues 594-1077), we have used RNA extracted from Human Embryonic Kidney 293 (HEK293T) and SH-SY5Y cells. RNA samples were extracted from 1 million cells using the RNeasy Mini Kit (Qiagen, 74136) and treated with TURBO DNA-freeTM Kit (Thermo Fisher Scientific, AM2238). Afterwards, 1 µg of RNA was reverse transcribed into cDNA using High-Capacity cDNA Reverse Transcription Kit (Thermo Fisher Scientific, 4368814). Primers used to amplify the FH2 domains of DAAM1 are provided in Table S1. The PCR product was cloned in pEMT33 (for actin polymerization assay and TIRF microscopy experiments) and in C145 pCoofy17 (for dual-color TIRF microscopy experiments), both vectors have been kindly provided by the Sebastian Maurer lab (CRG).

These constructs were expressed as fusion proteins with N-terminal IgG tag plus C-terminal Strep-tag in E. coli strain BL21-CodonPlus(DE3)-RIL strain (Agilent Technologies, 230245). Cells were cultured at 37°C until OD600nm reached 0.5, after which the media was cooled to 18°C and Isopropyl β-d-1-thiogalactopyranoside (IPTG; ROTH, 2316.1) was added to a final concentration of 0.1 mM to induce protein expression. Bacterial cultures were grown overnight at 18°C and subsequently harvested by centrifugation at 4°C (15 min, 4000 rpm) and disrupted by sonication. Sonication was conducted in HEKG 10 buffer (20 mM HEPES, pH 7.4, 1 mM EDTA, 50 mM KCl, 10% glycerol) with 1 mM DTT supplemented with cOmplete EDTA-free Protease Inhibitor Tablet (Sigma, 11873580001). After centrifugation (Eppendorf 5810R Centrifuge) at 4°C (20 min, 20000 rpm), proteins were purified using StrepTrap HP column (GE Healthcare, GE17-5248-01) at 4°C. The N-terminal tag was cleaved with His-C3 protease and the C-terminal tag with His-TEV protease (in house purified). Both proteases were further removed using Ni-NTA Agarose beads. Individual pooled DAAM1-FH2 proteins, with and without the microexon, were further purified by a passage through a Superose 6 column (GE Healthcare). Their concentration was evaluated using NanoDrop spectrophotometer (ThermoFisher) and their purity/integrity was assessed on SDS-PAGE, where coomassie staining (ThermoFisher, LC6065) was used for visualization.

Pyrene actin polymerization assays and TIRF microscopy

Pyrene-labeled actin protein (Universal Biologicals) was prepared as suggested by the manufacturer. In short, actin was equilibrated for 1 h at 4°C in G-buffer (5 mM Tris-HCl pH 8.0, 0.2 mM CaCl2) and spun for 30 min at 14 000 rpm before adding 10X Polymerization buffer (500 mM KCl, 20 mM MgCl2, 10 mM ATP) to a final 1X concentration. Actin assembly was measured in 60 µl reactions using 96 Well Black Polystyrene Microplates (Corning®, CLS3904). Pyrene fluorescence was monitored over time at 24°C at an excitation of 365 nm and emission of 407 nm in a fluorescence spectrophotometer (Tecan Infinite 200 PRO). Rates of actin assembly were calculated from the slope of the assembly curves at 50% polymerization (i.e., the time at which 50% of the actin has polymerized: half time). As described by (Doolittle, Rosen, and Padrick 2013), we computed the half time of each experiment based on the intensity values included in a specific interval. First, we calculated the average minimum intensity (average intensity of the 10 points closer to the minimum intensity) and the average maximum intensity (average intensity of the 10 points closer to tmax, where tmax is the average of the 10 points with highest intensity). Then, we used these values to compute the lower and higher bounds of the intensity interval used for the half time computation. The lower bound was defined as (0.5 - delta/2)*(avg_max_intensity - avg_min_intensity) + avg_min_intensity, while the higher bound was defined as (0.5 + delta/2)*(avg_max_intensity - avg_min_intensity) + avg_min_intensity (with delta=0.1, as recommended in (Doolittle, Rosen, and Padrick 2013)). Next, we used the points in each experiment with intensity values included between the lower and higher bounds to fit a linear model (intensity vs. time), and extracted the slope value returned by the fit. Finally, we derived the actin polymerization rate at the halftime by multiplying the slope value by a scaling factor (SF). SF was computed as (actin_conc - critical_conc)/(avg_max_intensity - avg_min_intensity), with actin_conc = 21.5 (actin original concentration), critical_conc = k_minus / k_plus. k_minus and k_plus represented the on-rate and off-rate constants for filament assembly, and were set at 1.4 and 11.6, respectively, as suggested by (Doolittle, Rosen, and Padrick 2013)).

TIRF-based F-actin polymerization experiments were performed using manually assembled flow-cells consisting of piranha-cleaned, silanized, PEG-passivated glass coverslips (22 X 22 mm #1.5 (i.e. 170 +/- 5 um) from MARIENFELD (Cat # 0107052)) and a PLL-PEG passivated slide (Consolati et al. 2022). Flow cells were primed by flushing 55 ul of a solution of 5% Pluronic F-127 (Sigma-Aldrich, P2443) and then incubated for 10 min at room temperature. Next, flow cells were washed twice with 55 ul of kappa-Casein (1:100 in 1X G-buffer of 5 mg/ml stock in 1X Brb80 buffer). Absorptive paper (Whatman filter paper) was used to flush the chamber by holding the paper on the outlet side of the channel while adding the solution dropwise in the inlet side. Chambers were then equilibrated with the G-buffer and the reaction mixture was loaded. The actin polymerization reaction mix contained the protein variant of interest (DAAM1-FH2 with or without microexon) and actin, which were diluted in freshly prepared buffer containing 5 mM Tris-HCl (pH 8.0), 0.2 mM CaCl2, 50 mM KCl, 2mM MgCl2, 2mM ATP, 2mM DTT, 1% (w/vol) glucose, 0.2 mM Brij-35, oxygen scavengers (180 mg/ml catalase (Merck, C40) and 752 mg/ml glucose oxidase (Serva, 22778.01)), 0.15% (w/vol) methylcellulose (Sigma-Aldrich, 4000 cP); actin labeling was achieved using SiR-Actin (TeuBio, SC001). After loading the reaction mixture, flow cells were finally sealed with vacuum grease and placed onto the microscope stage for observation. In order to minimize the experimental variations between the different conditions to be compared (actin alone, actin with +MIC and -MIC protein variants), experiments have been run in parallel, i.e. the three conditions were run simultaneously during each experiment. To this end, flow cells were divided into three separated channels using double sided tape.

TIRF imaging was performed with a custom assembled system (Cairn Research, Faversham, UK) built around an automated Nikon Eclipse Ti microscope equipped with a Perfect Focus System and an azimuthal TIRF unit (Gataca Systems, iLas2) using a 100X oil-immersion objective (Nikon CFI SR Apo, NA = 1.49), 488 nm and 640 nm simultaneous laser excitation at a TIRF angle of 80 deg, and two EMCCD cameras (Andor, iXon 888 Ultra) for fluorescent detection using a dichroic (Chroma, T565lpxr) to split the fluorescence onto the two cameras and a 525/50 bandpass filter (Chroma, 284337) for DAAM1-SNAP-Alexa488 detection and a 655 long-pass filter (Chroma, 283943) for SiR-actin detection. Imaging was performed at room temperature for 2 h taking 1 image every 2 min in 3 to 5 different sample locations chosen randomly and using 100 ms exposure time and 100 and 250 Electron Multiplying gain values, respectively for SiR-actin and DAAM1-SNAP-Atto488 detection.

TIRF-derived actin fluorescence micrographs were first denoised using rolling ball background subtraction (10 pixels), then contrast enhanced using the Frangi Vesselness filter (Frangi et al. 1998). From the acquired time series, actin images were skeletonized and analyzed using publicly available plugins (Arganda-Carreras et al. 2010; Polder, Hovens, and Zweers, 2010). The resulting skeleton label maps were used as reference locations for the quantification of the quantity (intensity) of protein bound to the actin fibers. SNAP-tag protein fluorescence images were denoised using rolling ball background subtraction (50 pixels) and the pixel statistics were calculated with CLIJ ImageJ/Fiji plugins (Haase et al. 2020). All the scripts were written in ImageJ/Fiji (Schindelin et al. 2012), and are available upon request.

Western Blot

Previously snap-frozen tissues or cell pellets were resuspended in RIPA buffer (150 mM NaCl, 1% Nonidet P-40, 1.0 mM EDTA, 1% Sodium Deoxycholate, 50mM Tris (pH 7.4)). The samples were subjected to sonication (1*10 sec pulse) and left on ice for 10 min. After centrifugation 5 min at 14000 rpm, the supernatants were collected and protein quantification determined using Bradford. Samples were resuspended in 4X SDS loading dye (200 mM Tris 6.8, 400 mM DTT, 4% SDS, 0.2% bromophenol blue, 20% glycerol), proteins were resolved by electrophoresis on a 10% SDS polyacrylamide gel and transferred on a nitrocellulose membrane. Blocking was performed in PBS 0.3% Tween, 5% milk. First antibody and secondary HRP labeled antibodies were diluted in the blocking buffer at a concentration provided in Table S2. Immunolabeling was detected by enhanced chemiluminescence and visualized with a digital luminescence image analyser Amersham Imager 600 (GE Healthcare).

Deletion of Daam1-MIC using CRISPR-Cas9 gene-editing

Mouse Embryonic Stem Cells (mESC, 129xC57Bl/6 background) were kindly provided by Kyung-Min Noh (EMBL Heidelberg) and cultured as described in Supplementary Methods. mESCs Knock-Out (KO) for the Daam1-MIC were generated using the CRISPR-Cas9 system (Ran et al. 2013) with a double guide RNA strategy (Sakuma et al. 2015). Each guide RNA targeted one of the two flanking introns and three gRNAs at each side were selected based on the proximity to Daam1-MIC and the quality score provided by (Doench et al. 2016). The best gRNA pair was chosen after testing all possible combinations and selecting the best editing efficiency. The primer sequences are provided in Table S1.

Gene editing was performed by transfection of 2 ug of Multiplex CRISPR vector ESCs with Lipofectamine 2000 (Invitrogen, 11668019). mESCs were plated at 2-3 different densities on 100 mm dishes (750 000, 1 500 000 and 3 000 000 cells/dish). Transfection of an empty vector was used as control. Six hours after transfection, the media was changed to prevent toxic effects. After 24h, puromycin selection was performed using a concentration of 1.5 ug/ml (Sigma, P8833), during 7 to 10 days. Afterwards, individual colonies were hand-picked into 96-well plates, expanded and genotyped by PCR and Sanger sequencing. Genotyping primer sequences are provided in Table S1. The confirmed KO clones and WT controls were further confirmed at the mRNA level using the RT-PCR primers amplifying Daam1-MIC described above.

Immunofluorescence stainings and confocal imaging of cultured neurons

Neuronal differentiation from mESCs was done following the protocol reported by Bibel et al., 2007, with slight modifications (see Supplementary Methods) (Bibel et al. 2004; 2007). For immunofluorescence assays, cells on DIV0 or on DIV21 were washed with phosphate-buffered saline (PBS), fixed in 4% paraformaldehyde in PBS for 10 min, permeabilized in 0.3% Triton X-100 in PBS for 10 min, blocked for 1 h in 0.3% Triton X-100, % bovine serum albumin (BSA) in PBS and incubated in primary antibodies at 4oC overnight with shaking. Following this incubation, cells were incubated with the corresponding secondary antibodies (see Table S2) for 1 h at room temperature and mounted in FluoroShield with DAPI (Sigma, F6057-20ml) for imaging. Images were taken on an SP8 confocal microscope (CRG, Advanced Light Microscopy Unit) using identical settings for each condition in a given experiment. Briefly: for IEG positive nuclei analysis (Figure; DIV21) and neurite length analysis (Figure ; DIV0+4h´s) dry 20X objective was used to image the whole span of the neuronal culture (17-23µm, Z-step size 1µm, zoom factor 2.5). For filopodia analysis 63X oil-immersion objective was used to image the whole span of the protrusion (around 2 µm, Z-step size 0.12 µm, zoom factor 2.5). Confocal sections were Z stack projected with maximum intensity selection and analyzed in ImageJ/Fiji software. Immediate early genes positive nuclei were counted using Analyze Particles plugin (nuclei size at least 25 pixel), and normalized to DAPI positive nuclei. Neurite and filopodia length were analyzed manually using the Segmented Line plugin.

Measurement of intracellular [Ca2+] in cultured neurons

Cytosolic Ca2+ signal was determined at room temperature in cells loaded with 4,5 mM FURA2-AM (30 min incubation at 37ºC). Ca2+ responses were calculated as the ratio of emitted fluorescence (510 nm) after excitation at 340 and 380 nm, relative to the ratio measured prior to cell stimulation (FURA2-AM ratio 340/380). Briefly, cells were maintained in an isotonic solution containing (in mM): 140 NaCl, 5 KCl, 1.2 CaCl2, 0.5 MgCl2, 5 glucose, 10 HEPES (305 mosmol/l, pH 7.4 with Tris) for 2 minutes and then stimulated with a 30 mM KCl isotonic solution (115 NaCl, 30 KCl, 1.2 CaCl2, 0.5 MgCl2, 5 glucose, 10 HEPES) to activate voltage-gated calcium entry. As indicated in the respective figure legends, cells were treated with 5 µM Latrunculin A (LatA), 50 µM small-molecule inhibitor of Formin Homology 2 domains (SMIFH2) or vehicle (DMSO). The treatment was maintained for the duration of the experiment (40 minutes). In the case of SMIFH2, its effect on neuronal cultures was measured after 90 min exposure to 50 µM SMIFH2. All experiments were carried out at room temperature as described previously (Fernandes et al. 2008). AquaCosmos software (Hamamatsu Photonics) was used for capturing the fluorescence ratio at 510 nm obtained post-excitation at 340 and 380 nm, respectively. Images were computed every 5 s. Measurements were processed using SigmaPlot 10 software.

Generation of mouse Daam1-MIC KO mice

Chimeric mice were obtained by blastocyst injection of one of the Daam1-MIC KO mESC lines into B6 albino (B6(Cg)-Tyrc-2J/J) embryos, which were then transferred to pseudopregnant CD1 females. Chimeric males were subsequently crossed to albino B6 females, and all non-albino mice were genotyped to select Daam1-MIC KO mice. These were backcrossed four times to C57Bl/6J and heterozygous mice were then crossed to generate Daam1-MIC KO and wild type (WT) littermates for experiments. The colony was maintained at the Animal Facility of the Barcelona Biomedical Research Park (PRBB). All procedures were approved by the PRBB Animal Research Ethics Committee and the Generalitat de Catalunya and were carried out in accordance with the guidelines of the European Union Council (2003/65/CE) and Spanish regulations (BOE 252/34367-91, 2005). WT mice were purchased from Charles River (references: 709 for albino B6, 022 for CD1 and 632 for C57Bl/6).

In Utero Cortical Electroporation

Cortical electroporation was performed as in García-Frigola et al. 2008 with minor changes. Timed-pregnant mouse females were anesthetized with isoflurane,the abdomen cut open and the uterine horns exposed. E15 wild-type embryos were unipolar injected into the ventricle using a pulled glass micropipette containing a DNA solution (1 µg/µl CAG-GFP plasmid (11150, Addgene) with 0.03% Fast Green in PBS). The head of each embryo was placed between tweezer-type electrodes (CUY650-P5 Nepa GENE, Chiba, Japan) and five square electric pulses (50 milliseconds) at 35V were passed at 950 msec. intervals using an electroporator (CUY21E, Nepa GENE). Then, electroporated brain cortex of PD4 mice were analyzed. PD4 mice were perfused with 4% PFA and brains cut in 70 µm slices using a vibratome device. GFP expressing neurons and their projections were visualized by immunohistochemistry with chicken anti-GFP antibody (Aves labs) and anti-chicken Alexa-488 secondary antibody (Invitrogene, Molecular Probes). 20x images were taken with Leica SPEII confocal microscope (two ROIs from 3 WT and 3 DAAM1-MIC) mice and the length of the primary dendrite was measured manually using FIJI software.

Functional synapse quantification in mice hippocampus

7 control mice and 8 DAAM1-MIC mice of 22 days postnatal (PD22) were perfused 5 minutes with 4% paraformaldehyde and brains were transferred to Phosphate Buffered Saline immediately. Brains were cut in 70µm sagittal slices, and equivalent slices between animals were selected for immunohistochemistry. Slices were placed in a blocking/permeabilization solution containing 5% horse serum and 0.25% Triton X-100 in PBS for 1 hour, followed by immunostaining with primary antibodies (Table S2) two days at 4°C. Slices were washed 4-5 times in PBS before staining with secondary antibodies (Table S2) overnight at 4°C. Slices were labeled with 4′,6-diamidino-2-phenylindole (DAPI) (Sigma-Aldrich, D9542) for 5 minutes and washed 3-4 times in PBS before being mounted in Mowiol mounting media (Millipore, 475904-M).

CA1 hippocampus was imaged with a 63x oil immersion objective on a Leica SPEII confocal microscope. ROIs with a z-stack of 5µm and a z-step size of 0.2µm were captured. Three ROIs per slice, and three slices per animal were analyzed with Imaris software. Images were processed with Background subtraction and Median filter for both channels, followed by segmentation with Imaris models. To quantify the number of functional synapses the “Spots Close To Surface XTension” of MatLab was applied with a threshold of 0.5µm.

DAAM1-MIC results were normalized to control mean and unpaired Mann-Whitney nonparametric test was performed for statistical analysis.

Immunohistochemical imaging of mice hippocampus

Mouse hippocampal sections were prepared as previously described (Hoeymissen et al. 2020). In brief, mice were euthanized with CO2, perfused transcardially with 0.1 M PBS followed by 4% paraformaldehyde in PBS until tissues were completely cleared of blood. Fixed brains were extracted and stored in 4% paraformaldehyde at 4 °C for 24 h, and in sucrose 30% with 0.01% azide in PBS for the following 24 h. Prepared tissues were cut into 40 µm coronal sections, in serial order throughout the dorsal hippocampus (Bregma sections between -1.34mm to -2.54mm). Sectioning was performed by an in house Tissue Engineering Unit (CRG). Immunohistochemistry was done by tissue permeabilization in 0.5% Triton X-100 in PBS for 15 min × 3 times, blocked for 2 h in 10% normal goat serum (NGS) in PBS albumin and incubated primary antibodies in 5% NGS, Tween 0.5% in PBS at 4oC overnight. Following this incubation, cells were incubated with the corresponding secondary antibodies (see Table S2) for 2 h at room temperature. Washing steps were repeated (for 15

min × 3 times) and sections were mounted in FluoroShield with DAPI for imaging. Images were taken on a confocal microscope (SP8 Leica; CRG, Advanced Light Microscopy Unit) using identical settings for each condition in a given experiment with a dry 20X objective. Single middle plane of each section was imaged and the images were analyzed in ImageJ/Fiji software. DG size was marked manually with Polygon selections using DAPI stained nuclei as a region of reference marker, and consecutively quantified with the Measure plugin. A detailed list of all stainings and primary antibodies used are provided in Table S2.

Behavioral and locomotor tests in a neonatal mice

A battery of behavioral and motor tests to probe early post-natal neurodevelopment was performed as described in Feather-Schussler and Ferguson (2016) and Roper et al. 2021, with some adjustments, as detailed in Supplementary Methods. In particular, we performed the following tests at PDs 4, 7, 10 and 14, unless stated otherwise: (i) Pivoting and walking, (ii) Righting reflex, (iii) Preyer's reflex, (iv) Front-limb suspension, (v) Hindlimb suspension, (vi) Grasping reflex, (vii) Cliff aversion, (viii) Negative geotaxis, (ix) Homing test.

Behavioral tests in Adult Mouse

We also performed a battery of behavioral and locomotors tests in adult mice. Each test was performed twice, using six animals per sex and genotype in each replicate. All mice were between 2 and 5 months old and siblings were matched when possible. As described in detailed in Supplementary Methods, we performed the following tests: (i) Spontaneous basal locomotor activity, (ii) Novel Object Recognition (NOR), (iii) Elevated Plus Maze, (iv) Morris Water Maze, (v) Grip strength, (vi) Rotarod, (vi) Beam Balance, (vii) Fear conditioning.

Electrophysiology ex vivo

Mice (8–16 week old) were decapitated immediately, the brain was quickly removed and submerged in artificial cerebrospinal fluid rich in aCSF sucrose buffer (2 mM KCl, 1.25 mM NaH2PO4-H2O, 7 mM MgSO4, 26 mM NaHCO3, 0.5 mM CaCl2, 10 mM glucose and 219 mM sucrose) at 4°C, saturated with a 95% O2, 5% CO2 mixture and maintained at pH 7.32-7.4. Transverse brain slices (300 µm thick) were cut with a vibratome (VT1200S, Leica) in oxygenated aCSF sucrose at 4°C and transferred to recovery chamber with oxygenated aCSF buffer 124 mM NaCl, 2.5 mM KCl, 1.25 mM NaH2PO4-H2O, 1 mM MgSO4, 26 mM NaHCO3, 2 mM CaCl2 and 10 mM glucose and incubated for > 1 h at room temperature (21-24 ºC) and pH 7.32-7.4. Individual slices were transferred to an immersion recording chamber and perfused with oxygenated aCSF at 2 mL/min (30 ± 2°C).

Whole-cell intracellular recordings in voltage clamp (VC) and current clamp (CC) mode were performed in pyramidal neurons in CA1 stratum pyramidale. Cells were visualized with a water-immersion 40x objective. Patch electrodes were fabricated from borosilicate glass capillaries (P1000, Sutter Instrument) with resistance of 4–6 MΩ when filled with the internal solution that contained : 130 mM K-MeSO4, 10 mM HEPES, 0.5 mM EGTA, 2 mM MgCl2, 4 mM Mg-ATP, 0.4 mM Na-GTP, 10 mM phosphocreatin di (tris) salt and 0.3 % biocytin, for membrane properties experiments in CC and excitatory postsynaptic currents (EPSC) evoked in VC, in pyramidal neurons; 130 mM Cs-MeSO4, 5 mM CsCl, 10 mM HEPES, 0.5 mM EGTA, 2 mM MgCl2, 4 mM Mg-ATP, 0.4 mM Na-GTP, 10 mM phosphocreatin di (tris) salt and 0.3 % biocytin, for miniature excitatory postsynaptic currents (mEPSC) in VC recordings from pyramidal neurons. All pipette solutions were adjusted to pH 7.2-7.3 with K-OH or Cs-OH. Membrane currents and voltages were acquired with Multiclamp 700B amplifiers, digitized (Digidata 1550B) and controlled by pClamp 10.7 (Molecular Devices Corporation, Sunnyvale, CA, USA) software. Membrane intrinsic properties of CA1 pyramidal cells were determined by passing hyperpolarizing and depolarizing current steps (1 s, with 10 pA increments from -100 to 140 pA) in CC.

Synaptic responses in CA1 were evoked by monophasic current (50 µs duration) stimulation of the Schaffer collateral fibers (SCs) with an extracellular bipolar tungsten electrode via isolated current stimulator (DS3) that was set to deliver monophasic currents of 50 µs duration. Membrane currents and voltages were acquired with Multiclamp 700B amplifiers, digitized (Digidata 1550B) and controlled by pClamp 10.7 (Molecular Devices Corporation, Sunnyvale, CA, USA) software. To study changes in the probability of transmitter release of the presynaptic cell (e.g., Bekkers and Stevens 1990; Kullmann 1994; Malinow and Tsien 1990) we applied paired-pulse facilitation (PPF) protocol, which consisted of evoking two consecutive EPSC responses at different intervals (from 20 ms at 160 ms, a 20 ms inter-pulse interval). Changes in the PPF were calculated as a PPF ratio from (R2-R1)/R1, where R1 and R2 were the peak amplitudes of the first and second EPSCs, respectively (Martin and Buño, 2002). Extracellular field postsynaptic potentials (fEPSPs) were recorded by placing borosilicate glass electrode filled with aSCF sucrose buffer in the stratum radiatum (SR) of the CA1 pyramidal layer. Evoked fEPSPs were elicited by stimulation of the SCs fibers as EPSCs.

For LTP experiments, the stimulus intensity was adjusted to elicit 50% of the maximum response signal and kept constant throughout the experiment. Data was stored through an acquisition system (Axon Instruments) and the software pClamp 10.7 was used to display fEPSP and measurements of fEPSP slopes. After recording stable baseline responses for 30 min, LTP was induced by a single train of theta burst stimulation (TBS; 10 bursts of 5 pulses at 100 Hz, with an interval of 200 ms between bursts). Potentiation was measured for 1 h after LTP induction at 0.033 Hz. Changes in the fEPSP slope were calculated in relation to the baseline fEPSP responses during the last 10 min before TBS, and the time course of LTP values was then normalized to this baseline.

Dendritic spine morphology analysis

For spine analysis, neurons were filled with biocytin (Sigma-B4261) during whole-cell recordings. Slices (300 µm) with recorded cells were fixed overnight with 4% paraformaldehyde in PBS at 4°C and then transferred to 0.05 % Na-azide in PBS. After slices were permeabilized and blocked with 0.3% Triton X-100 in PBS and 10% normal goat serum (NGS) for 1 h at room temperature. To reveal biocytin, the slices were incubated overnight at 4°C with streptavidin Alexa Fluor-488 conjugated (1:1 000) in 0.3% Triton X-100 in PBS. Confocal microscopy (Leica SP8; CRG, Advanced Light Microscopy Unit) was used to capture fluorescence Z-stacks of dendritic spines from biocytin filled cells with a 0.2 µm step using a 63X glycerol immersion objective. Only dendrites with bright and continuous labeling were included for analysis. Primary dendrites were not included in the analysis. Huygens' essential software was used to deconvolve images. All images were batch processed using the same template (available upon request). Deconvoluted images were imported into NeuronStudio and semi-automatically analyzed blind to experimental conditions. Dendritic spine quantification was performed on a total of 23 CA1 pyramidal cells (n = 11-12 cells per group; n = 2 groups). Spine density was measured at least in 100 µm of secondary apical branches. All dendritic spines were at least 50 µm apart from the neuronal soma. The total number of spines was divided by the total length of the dendritic spines.

RhoA2G FRET biosensor analysis of neuronal cells by microscopy

To obtain lentivirus for infection of neurons, HEK293T cells were seeded in lentivirus packaging media (94.99% Opti-MEM I, 5% FBS,0.01% Sodium Pyruvate) were transfected according to manufacturer instructions using Lipofectamine 2000 with plasmids carrying HIV-1 Gag/Pol (pMDLg/pRRE Addgene: 12251), HIV-1 Rev (pRSV-Rev Addgene: 12253), and VSV g-glycoprotein Env (pMD2.G Addgene: 12259), together with pLentiRhoA2G (Addgene: 40179). Media was changed after 6 h to neuronal N2 media. The viral particles were harvested from the neuronal N2 media 48 h after the transfection and used for cell infection. Experiment was performed on two separate neuronal differentiations considered as replicates. Each differentiation was performed using three KO and three WT cell lines (described before), and fixed DIV21 neurons were used for FRET analysis. Procedure was performed in accordance with safety rules and approved by the CRG Biosafety committee (procedure registration number CBS19_015_A).

Relative FRET was calculated automatically using AcceptorPhotobleaching (confocal microscope SP8 Leica; CRG, Advanced Light Microscopy Unit) by dividing the normalized fluorescence intensity of Venus at its emission peak (528 nm) by the normalized fluorescence intensity of mTFP1 at its emission peak (492 nm). Provided Lookup Table (LUT) is linear and covers the full range of the data.

RNA-sequencing and transcriptomic analyses

Mice (age 3-5 months) were euthanized with CO2 and decapitated immediately. Hippocampi from 10 mice (5 per genotype) were extracted, snap-frozen in liquid nitrogen and subjected to RNA extraction using the RNeasy Plus Mini kit (Qiagen, 74136). Library preparation (polyA-selected, stranded) and the RNA-seq were performed by the CRG Genomics Core Facility following standard Illumina protocols. An average of 29.3 million 50 bp single-end reads were generated for each library on a Illumina HiSeq 2500 machine.

Reads were aligned to the Mus musculus transcriptome assembly from Ensembl (release 104; GRCm39) with Salmon v.1.4.0 (Patro et al. 2017). Raw gene counts were extracted from Salmon outputs using tximport (Soneson, Love, and Robinson 2015) package from bioconductor and differential gene expression was assessed with DESeq2 (Love, Huber, and Anders 2014). Log2 fold changes between KO and WT were shrunk using apeglm method (Zhu, Ibrahim, and Love 2019) and used for plotting KEGG pathways with the bioconductor package pathview (Luo and Brouwer 2013). Gene expression was transformed with variance stabilizing transformations (VST) as implemented in DESeq2 and used as input for the Gene Set Variation Analysis (Hänzelmann, Castelo, and Guinney 2013) on KEGG pathways. Gene sets were considered differentially expressed if p-value was lower than 0.05 in a linear model modeling for genotype. RNA-seq data have been deposited in the Gene Expression Omnibus (GEO), and is available at the GSE219244 accession number.

End Matter

Author Contributions and Notes

P.P performed molecular, cellular, and behavioral characterization of the microexon function, with help of M.M.C. A.Z.M generated and analyzed electrophysiology data (Figure 6 and S8); F.M. performed the analysis of the actin polymerization assay, provided support with bioinformatic analyses and contributed with critical insights. G.C.R performed calcium imaging experiments and the analysis. D.N. performed TIRF and dual-color TIRF microscopy experiments and R.G.R. wrote ImageJ/Fiji scripts necessary for the downstream analysis. L.I.R. analyzed RNA-seq data, and provided help with animal behavior data analysis. C.M.P and P.O.C. performed functional synapse quantification (Figure 4) and neuronal complexity analysis (Figure S5). S.B. performed Western Blot analysis and contributed with critical insights. C.R.-M. and J.P. performed RT-PCR assays and genotyping. M.M. De L.C., Á.F.-B., C.S., J.L.M.L., and O.F. provided support for the animal experiments performed. D.L. and J.I.W.F. helped with FRET acceptor photobleaching experiments.P.P., E.H., M.D., and M.I designed the experiments with input from other authors. P.P., M.D. and M.I. conceived the study, supervised the work and wrote the manuscript with input from other authors.

The authors declare no conflict of interest.

Acknowledgments

We thank Kyung-Min Noh for providing the mESC line, Miguel Valverde and Francisco Muñoz for their help and feedback with the calcium imaging experiments, and members of the Irimia and Dierssen groups for constant scientific discussion and feedback. We also thank the CRG Genomics, Protein Technologies, Tissue Engineering and Advanced Light Microscopy Units for the RNA sequencing, protein purification, blastocyst injection and microscopy services, respectively.

Funding statement

The research has been funded by the European Research Council (ERC) under the European Union's Horizon 2020 research and innovation program (ERC-StG-LS2-637591 and ERCCoG-LS2-101002275 to M.I.), the Spanish Ministry of Economy and Competitiveness (BFU-2017-89201-P to M.I.) and the 'Centro de Excelencia Severo Ochoa 2013-2017'(SEV-2012-0208). P.P. has received funding from the European Union's Horizon 2020 research and innovation programme under the Marie Sklodowska-Curie grant agreement No 721890 (ITN circRTrain).

References

Barbosa-Morais, N. L., M. Irimia, Q. Pan, H. Y. Xiong, S. Gueroussov, L. J. Lee, V. Slobodeniuc, et al. 2012. "The Evolutionary Landscape of Alternative Splicing in Vertebrate Species." *Science* 338 (6114): 1587–93. https://doi.org/10.1126/science.1230612.

Bibel, Miriam, Jens Richter, Emmanuel Lacroix, and Yves-Alain Barde. 2007. "Generation of a Defined and Uniform Population of CNS Progenitors and Neurons from Mouse Embryonic Stem Cells." *Nature Protocols* 2 (5): 1034–43. https://doi.org/10.1038/nprot.2007.147.

Bibel, Miriam, Jens Richter, Katrin Schrenk, Kerry Lee Tucker, Volker Staiger, Martin Korte, Magdalena Goetz, and Yves-Alain Barde. 2004. "Differentiation of Mouse Embryonic Stem Cells into a Defined Neuronal Lineage." *Nature Neuroscience* 7 (9): 1003–9. https://doi.org/10.1038/nn1301.

Bramham, Clive R., Maria N. Alme, Margarethe Bittins, Sjoukje D. Kuipers, Rajeevkumar R. Nair, Balagopal Pai, Debabrata Panja, et al. 2010. "The Arc of Synaptic Memory." *Experimental Brain Research* 200 (2): 125–40. https://doi.org/10.1007/s00221-009-1959-2.

Calarco, John A., Simone Superina, Dave O'Hanlon, Mathieu Gabut, Bushra Raj, Qun Pan, Ursula Skalska, et al. 2009. "Regulation of Vertebrate Nervous System Alternative Splicing and Development by an SR-Related Protein." *Cell* 138 (5): 898–910. https://doi.org/10.1016/j.cell.2009.06.012.

Ciampi, Ludovica, Federica Mantica, Laura López-Blanch, Jon Permanyer, Cristina Rodriguez-Marín, Jingjing Zang, Damiano Cianferoni, et al. 2022. "Specialization of the Photoreceptor Transcriptome by *Srrm3* -Dependent Microexons Is Required for Outer Segment Maintenance and Vision." *Proceedings of the National Academy of Sciences* 119 (29): e2117090119. https://doi.org/10.1073/pnas.2117090119.

Cingolani, Lorenzo A., and Yukiko Goda. 2008. "Actin in Action: The Interplay between the Actin Cytoskeleton and Synaptic Efficacy." *Nature Reviews Neuroscience* 9 (5): 344–56. https://doi.org/10.1038/nrn2373.

Consolati, Tanja, Gil Henkin, Johanna Roostalu, and Thomas Surrey. 2022. "Real-Time Imaging of Single ΓTuRC-Mediated Microtubule Nucleation Events In Vitro by TIRF Microscopy." In *Microtubules*, edited by Hiroshi Inaba, 2430:315–36. Methods in Molecular Biology. New York, NY: Springer US. https://doi.org/10.1007/978-1-0716-1983-4_21.

Dillon, Christian, and Yukiko Goda. 2005. "THE ACTIN CYTOSKELETON: Integrating Form and Function at the Synapse." *Annual Review of Neuroscience* 28 (1): 25–55. https://doi.org/10.1146/annurev.neuro.28.061604.135757.

Doench, John G, Nicolo Fusi, Meagan Sullender, Mudra Hegde, Emma W Vaimberg, Katherine F Donovan, Ian Smith, et al. 2016. "Optimized SgRNA Design to Maximize Activity and Minimize Off-Target Effects of CRISPR-Cas9." *Nature Biotechnology* 34 (2): 184–91. https://doi.org/10.1038/nbt.3437.

Doolittle, Lynda K., Michael K. Rosen, and Shae B. Padrick. 2013. "Measurement and Analysis of In Vitro Actin Polymerization." In *Adhesion Protein Protocols*, edited by Amanda S. Coutts, 1046:273–93. Totowa, NJ: Humana Press. https://doi.org/10.1007/978-1-62703-538-5_16.

Feather-Schussler, Danielle N., and Tanya S. Ferguson. 2016. "A Battery of Motor Tests in a Neonatal Mouse Model of Cerebral Palsy." *Journal of Visualized Experiments*, no. 117 (November): 53569. https://doi.org/10.3791/53569.

Feng, Dairong, and Jiuyong Xie. 2013. "Aberrant Splicing in Neurological Diseases: Aberrant Splicing in Neurological Diseases." *Wiley Interdisciplinary Reviews: RNA* 4 (6): 631–49. https://doi.org/10.1002/wrna.1184.

Fernandes, Jacqueline, Ivan M. Lorenzo, Yaniré N. Andrade, Anna Garcia-Elias, Selma A. Serra, José M. Fernández-Fernández, and Miguel A. Valverde. 2008. "IP3 Sensitizes TRPV4 Channel to the Mechano- and Osmotransducing Messenger 5′-6′-Epoxyeicosatrienoic Acid." *Journal of Cell Biology* 181 (1): 143–55. https://doi.org/10.1083/jcb.200712058.

Fritz, Rafael D., Michel Letzelter, Andreas Reimann, Katrin Martin, Ludovico Fusco, Laila Ritsma, Bas Ponsioen, et al. 2013. "A Versatile Toolkit to Produce Sensitive FRET Biosensors to Visualize Signaling in Time and Space." *Science Signaling* 6 (285). https://doi.org/10.1126/scisignal.2004135.

Gao, Chan, and Ye-Guang Chen. 2010. "Dishevelled: The Hub of Wnt Signaling." *Cellular Signalling* 22 (5): 717–27. https://doi.org/10.1016/j.cellsig.2009.11.021.

García-Frigola, Cristina, Maria Isabel Carreres, Celia Vegar, Carol Mason, and Eloísa Herrera. 2008. "Zic2 Promotes Axonal Divergence at the Optic Chiasm Midline by EphB1-Dependent and -Independent Mechanisms." *Development* 135 (10): 1833–41. https://doi.org/10.1242/dev.020693.

Gonatopoulos-Pournatzis, Thomas, and Benjamin J Blencowe. 2020. "Microexons: At the Nexus of Nervous System Development, Behaviour and Autism Spectrum Disorder." *Current Opinion in Genetics & Development* 65 (December): 22–33. https://doi.org/10.1016/j.gde.2020.03.007.

Gonatopoulos-Pournatzis, Thomas, Mingkun Wu, Ulrich Braunschweig, Jonathan Roth, Hong Han, Andrew J. Best, Bushra Raj, et al. 2018. "Genome-Wide CRISPR-Cas9 Interrogation of Splicing Networks

Reveals a Mechanism for Recognition of Autism-Misregulated Neuronal Microexons." *Molecular Cell* 72 (3): 510-524.e12. https://doi.org/10.1016/j.molcel.2018.10.008.

Habas, Raymond, Yoichi Kato, and Xi He. 2001. "Wnt/Frizzled Activation of Rho Regulates Vertebrate Gastrulation and Requires a Novel Formin Homology Protein Daam1." *Cell* 107 (7): 843–54.

Higashi, Tomohito, Tomoyuki Ikeda, Ryutaro Shirakawa, Hirokazu Kondo, Mitsunori Kawato, Masahito Horiguchi, Tomohiko Okuda, et al. 2008. "Biochemical Characterization of the Rho GTPase-Regulated Actin Assembly by Diaphanous-Related Formins, MDia1 and Daam1, in Platelets." *Journal of Biological Chemistry* 283 (13): 8746–55. https://doi.org/10.1074/jbc.M707839200.

Irimia, Manuel, Robert J. Weatheritt, Jonathan D. Ellis, Neelroop N. Parikshak, Thomas Gonatopoulos-Pournatzis, Mariana Babor, Mathieu Quesnel-Vallières, et al. 2014. "A Highly Conserved Program of Neuronal Microexons Is Misregulated in Autistic Brains." *Cell* 159 (7): 1511–23. https://doi.org/10.1016/j.cell.2014.11.035.

Jaiswal, Richa, Dennis Breitsprecher, Agnieszka Collins, Ivan R. Corrêa, Ming-Qun Xu, and Bruce L. Goode. 2013. "The Formin Daam1 and Fascin Directly Collaborate to Promote Filopodia Formation." *Current Biology* 23 (14): 1373–79. https://doi.org/10.1016/j.cub.2013.06.013.

Kawabata Galbraith, Kelly, Kazuto Fujishima, Hiroaki Mizuno, Sung-Jin Lee, Takeshi Uemura, Kenji Sakimura, Masayoshi Mishina, Naoki Watanabe, and Mineko Kengaku. 2018. "MTSS1 Regulation of Actin-Nucleating Formin DAAM1 in Dendritic Filopodia Determines Final Dendritic Configuration of Purkinje Cells." *Cell Reports* 24 (1): 95-106.e9. https://doi.org/10.1016/j.celrep.2018.06.013.

Kühn, Sonja, and Matthias Geyer. 2014. "Formins as Effector Proteins of Rho GTPases." *Small GTPases* 5 (3): e983876. https://doi.org/10.4161/sgtp.29513.

Lamprecht, Raphael. 2021. "Actin Cytoskeleton Role in the Maintenance of Neuronal Morphology and Long-Term Memory." *Cells* 10 (7): 1795. https://doi.org/10.3390/cells10071795.

Leger, Marianne, Anne Quiedeville, Valentine Bouet, Benoît Haelewyn, Michel Boulouard, Pascale Schumann-Bard, and Thomas Freret. 2013. "Object Recognition Test in Mice." *Nature Protocols* 8 (12): 2531–37. https://doi.org/10.1038/nprot.2013.155.

Love, Michael I, Wolfgang Huber, and Simon Anders. 2014. "Moderated Estimation of Fold Change and Dispersion for RNA-Seq Data with DESeq2." *Genome Biology* 15 (12): 550. https://doi.org/10.1186/s13059-014-0550-8.

Lu, Jun, Wuyi Meng, Florence Poy, Sankar Maiti, Bruce L. Goode, and Michael J. Eck. 2007. "Structure of the FH2 Domain of Daam1: Implications for Formin Regulation of Actin Assembly." *Journal of Molecular Biology* 369 (5): 1258–69. https://doi.org/10.1016/j.jmb.2007.04.002.

Lueptow, Lindsay M. 2017. "Novel Object Recognition Test for the Investigation of Learning and Memory in Mice." *Journal of Visualized Experiments*, no. 126 (August): 55718. https://doi.org/10.3791/55718.

Luo, Weijun, and Cory Brouwer. 2013. "Pathview: An R/Bioconductor Package for Pathway-Based Data Integration and Visualization." *Bioinformatics* 29 (14): 1830–31. https://doi.org/10.1093/bioinformatics/btt285.

Mattila, Pieta K, and Pekka Lappalainen. 2008. "Filopodia: Molecular Architecture and Cellular Functions," 9.

Matusek, T., R. Gombos, A. Szecsenyi, N. Sanchez-Soriano, A. Czibula, C. Pataki, A. Gedai, A. Prokop, I. Rasko, and J. Mihaly. 2008. "Formin Proteins of the DAAM Subfamily Play a Role during Axon Growth." *Journal of Neuroscience* 28 (49): 13310–19. https://doi.org/10.1523/JNEUROSCI.2727-08.2008.

McLeod, Faye, and Patricia C Salinas. 2018. "Wnt Proteins as Modulators of Synaptic Plasticity." *Current Opinion in Neurobiology* 53 (December): 90–95. https://doi.org/10.1016/j.conb.2018.06.003.

Messaoudi, E., T. Kanhema, J. Soule, A. Tiron, G. Dagyte, B. da Silva, and C. R. Bramham. 2007. "Sustained Arc/Arg3.1 Synthesis Controls Long-Term Potentiation Consolidation through Regulation of Local Actin Polymerization in the Dentate Gyrus In Vivo." *Journal of Neuroscience* 27 (39): 10445–55. https://doi.org/10.1523/JNEUROSCI.2883-07.2007.

Nakaya, Masa-aki, Kristibjorn Orri Gudmundsson, Yuko Komiya, Jonathan R. Keller, Raymond Habas, Terry P. Yamaguchi, and Rieko Ajima. 2020. "Placental Defects Lead to Embryonic Lethality in Mice Lacking the Formin and PCP Proteins Daam1 and Daam2." Edited by Michael Schubert. *PLOS ONE* 15 (4): e0232025. https://doi.org/10.1371/journal.pone.0232025.

Okuno, Hiroyuki, Kaori Akashi, Yuichiro Ishii, Nan Yagishita-Kyo, Kanzo Suzuki, Mio Nonaka, Takashi Kawashima, et al. 2012. "Inverse Synaptic Tagging of Inactive Synapses via Dynamic Interaction of Arc/Arg3.1 with CaMKIIβ." *Cell* 149 (4): 886–98. https://doi.org/10.1016/j.cell.2012.02.062.

Otomo, Takanori, Diana R Tomchick, Chinatsu Otomo, Sanjay C Panchal, Mischa Machius, and Michael K Rosen. 2005. "Structural Basis of Actin FIlament Nucleation and Processive Capping by a Formin Homology 2 Domain" 433: 7.

Pan, Qun, Ofer Shai, Leo J Lee, Brendan J Frey, and Benjamin J Blencowe. 2008. "Deep Surveying of Alternative Splicing Complexity in the Human Transcriptome by High-Throughput Sequencing." *Nature Genetics* 40 (12): 1413–15. https://doi.org/10.1038/ng.259.

Papandréou, Marie-Jeanne, and Christophe Leterrier. 2018. "The Functional Architecture of Axonal Actin." *Molecular and Cellular Neuroscience* 91 (September): 151–59. https://doi.org/10.1016/j.mcn.2018.05.003.

Parras, Alberto, Héctor Anta, María Santos-Galindo, Vivek Swarup, Ainara Elorza, José L. Nieto-González, Sara Picó, et al. 2018. "Autism-like Phenotype and Risk Gene MRNA Deadenylation by CPEB4 Mis-Splicing." *Nature* 560 (7719): 441–46. https://doi.org/10.1038/s41586-018-0423-5.

Plath, Niels, Ora Ohana, Björn Dammermann, Mick L. Errington, Dietmar Schmitz, Christina Gross, Xiaosong Mao, et al. 2006. "Arc/Arg3.1 Is Essential for the Consolidation of Synaptic Plasticity and Memories." *Neuron* 52 (3): 437–44. https://doi.org/10.1016/j.neuron.2006.08.024.

Polder, Gerrit, Huub Hovens, and Hans Zweers. n.d. "Measuring Shoot Length of Submerged Aquatic Plants Using Graph Analysis," 30.

Pollard, Thomas D. 2016. "Actin and Actin-Binding Proteins." *Cold Spring Harbor Perspectives in Biology* 8 (8): a018226. https://doi.org/10.1101/cshperspect.a018226.

Quesnel-Vallières, Mathieu, Zahra Dargaei, Manuel Irimia, Thomas Gonatopoulos-Pournatzis, Joanna Y. Ip, Mingkun Wu, Timothy Sterne-Weiler, et al. 2016. "Misregulation of an Activity-Dependent Splicing Network as a Common Mechanism Underlying Autism Spectrum Disorders." *Molecular Cell* 64 (6): 1023–34. https://doi.org/10.1016/j.molcel.2016.11.033.

Raj, Bushra, Manuel Irimia, Ulrich Braunschweig, Timothy Sterne-Weiler, Dave O'Hanlon, Zhen-Yuan Lin, Ginny I. Chen, et al. 2014. "A Global Regulatory Mechanism for Activating an Exon Network Required for Neurogenesis." *Molecular Cell* 56 (1): 90–103. https://doi.org/10.1016/j.molcel.2014.08.011.

Ran, F Ann, Patrick D Hsu, Jason Wright, Vineeta Agarwala, David A Scott, and Feng Zhang. 2013. "Genome Engineering Using the CRISPR-Cas9 System." *Nature Protocols* 8 (11): 2281–2308. https://doi.org/10.1038/nprot.2013.143.

Rial Verde, Emiliano M., Jane Lee-Osbourne, Paul F. Worley, Roberto Malinow, and Hollis T. Cline. 2006. "Increased Expression of the Immediate-Early Gene Arc/Arg3.1 Reduces AMPA Receptor-Mediated Synaptic Transmission." *Neuron* 52 (3): 461–74. https://doi.org/10.1016/j.neuron.2006.09.031.

Roper, Randall J., Charles R. Goodlett, María Martínez de Lagrán, and Mara Dierssen. 2020. "Behavioral Phenotyping for Down Syndrome in Mice." *Current Protocols in Mouse Biology* 10 (3): e79. https://doi.org/10.1002/cpmo.79.

Ruhela, Rakesh K, Shringika Soni, Phulen Sarma, Ajay Prakash, and Bikash Medhi. 2019. "Negative Geotaxis: An Early Age Behavioral Hallmark to VPA Rat Model of Autism." *Annals of Neurosciences* 26 (1): 25–31. https://doi.org/10.5214/ans.0972.7531.260106.

Sakuma, Tetsushi, Ayami Nishikawa, Satoshi Kume, Kazuaki Chayama, and Takashi Yamamoto. 2015. "Multiplex Genome Engineering in Human Cells Using All-in-One CRISPR/Cas9 Vector System." *Scientific Reports* 4 (1). https://doi.org/10.1038/srep05400.

Schindelin, Johannes, Ignacio Arganda-Carreras, Erwin Frise, Verena Kaynig, Mark Longair, Tobias Pietzsch, Stephan Preibisch, et al. 2012. "Fiji: An Open-Source Platform for Biological-Image Analysis." *Nature*

Methods 9 (7): 676–82. https://doi.org/10.1038/nmeth.2019.
Schönichen, André, and Matthias Geyer. 2010. "Fifteen Formins for an Actin Filament: A Molecular View on the Regulation of Human Formins." *Biochimica et Biophysica Acta (BBA) - Molecular Cell Research* 1803 (2): 152–63. https://doi.org/10.1016/j.bbamcr.2010.01.014.
Shen, Wenjuan, Michaela B. C. Kilander, Morgan S. Bridi, Jeannine A. Frei, Robert F. Niescier, Shiyong Huang, and Yu‐Chih Lin. 2020. "Tomosyn Regulates the Small RhoA GTPase to Control the Dendritic Stability of Neurons and the Surface Expression of AMPA Receptors." *Journal of Neuroscience Research* 98 (6): 1213–31. https://doi.org/10.1002/jnr.24608.
Soneson, Charlotte, Michael I. Love, and Mark D. Robinson. 2015. "Differential Analyses for RNA-Seq: Transcript-Level Estimates Improve Gene-Level Inferences." *F1000Research* 4 (December): 1521. https://doi.org/10.12688/f1000research.7563.1.
Szikora, Szilárd, István Földi, Krisztina Tóth, Ede Migh, Andrea Vig, Beáta Bugyi, József Maléth, et al. 2017. "The Formin DAAM Is Required for Coordination of the Actin and Microtubule Cytoskeleton in Axonal Growth Cones." *Journal of Cell Science*, January, jcs.203455. https://doi.org/10.1242/jcs.203455.
Tapial, Javier, Kevin C.H. Ha, Timothy Sterne-Weiler, André Gohr, Ulrich Braunschweig, Antonio Hermoso-Pulido, Mathieu Quesnel-Vallières, et al. 2017. "An Atlas of Alternative Splicing Profiles and Functional Associations Reveals New Regulatory Programs and Genes That Simultaneously Express Multiple Major Isoforms." *Genome Research* 27 (10): 1759–68. https://doi.org/10.1101/gr.220962.117.
Tomás Pereira, Inês, and Rebecca D. Burwell. 2015. "Using the Spatial Learning Index to Evaluate Performance on the Water Maze." *Behavioral Neuroscience* 129 (4): 533–39. https://doi.org/10.1037/bne0000078.
Torres-Méndez. 2022. "Parallel Evolution of a Splicing Program Controlling Neuronal Excitability in Flies and Mammals." *SCIENCE ADVANCES*, 20.
Torres-Méndez, Antonio, Sophie Bonnal, Yamile Marquez, Jonathan Roth, Marta Iglesias, Jon Permanyer, Isabel Almudí, et al. 2019. "A Novel Protein Domain in an Ancestral Splicing Factor Drove the Evolution of Neural Microexons." *Nature Ecology & Evolution* 3 (4): 691–701. https://doi.org/10.1038/s41559-019-0813-6.
Vorhees, Charles V, and Michael T Williams. 2006. "Morris Water Maze: Procedures for Assessing Spatial and Related Forms of Learning and Memory." *Nature Protocols* 1 (2): 848–58. https://doi.org/10.1038/nprot.2006.116.
Walf, Alicia A, and Cheryl A Frye. 2007. "The Use of the Elevated plus Maze as an Assay of Anxiety-Related Behavior in Rodents." *Nature Protocols* 2 (2): 322–28. https://doi.org/10.1038/nprot.2007.44.
Wang, Eric T., Rickard Sandberg, Shujun Luo, Irina Khrebtukova, Lu Zhang, Christine Mayr, Stephen F. Kingsmore, Gary P. Schroth, and Christopher B. Burge. 2008. "Alternative Isoform Regulation in Human Tissue Transcriptomes." *Nature* 456 (7221): 470–76. https://doi.org/10.1038/nature07509.
Warburton, E.C., and M.W. Brown. 2015. "Neural Circuitry for Rat Recognition Memory." *Behavioural Brain Research* 285 (May): 131–39. https://doi.org/10.1016/j.bbr.2014.09.050.
Xu, Yingwu, James B Moseley, Isabelle Sagot, Florence Poy, David Pellman, Bruce L Goode, and Michael J Eck. n.d. "Crystal Structures of a Formin Homology-2 Domain Reveal a Tethered Dimer Architecture," 13.
Yamashita, Masami, Tomohito Higashi, Shiro Suetsugu, Yusuke Sato, Tomoyuki Ikeda, Ryutaro Shirakawa, Toru Kita, et al. 2007. "Crystal Structure of Human DAAM1 Formin Homology 2 Domain: DAAM1 FH2 Structure." *Genes to Cells* 12 (11): 1255–65. https://doi.org/10.1111/j.1365-2443.2007.01132.x.
Zhang, Haorui, Youssif Ben Zablah, Haiwang Zhang, and Zhengping Jia. 2021. "Rho Signaling in Synaptic Plasticity, Memory, and Brain Disorders." *Frontiers in Cell and Developmental Biology* 9 (October): 729076. https://doi.org/10.3389/fcell.2021.729076.
Zhang, Hongyu, and Clive R. Bramham. 2021. "Arc/Arg3.1 Function in Long‐term Synaptic Plasticity: Emerging Mechanisms and Unresolved Issues." *European Journal of Neuroscience* 54 (8): 6696–6712. https://doi.org/10.1111/ejn.14958.

Supplementary figures

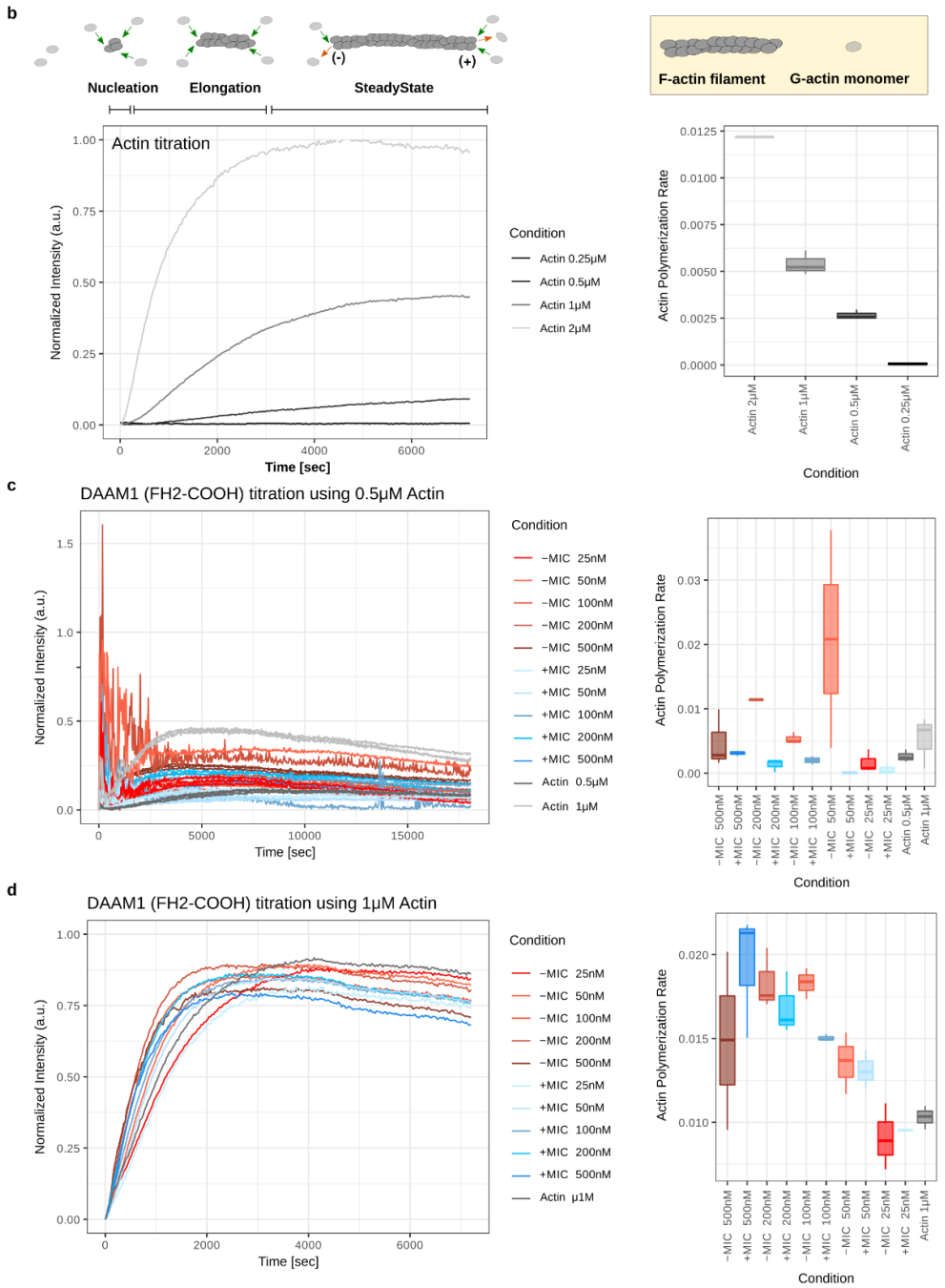

Supplementary Figure 1 - Linker region conservation among formins and actin pyrene assay optimization. (a) Amino acid sequence alignment of the linker regions of formin proteins. (b) Concentration-dependent actin self-assembly. Left: actin self-assembly measured by incubation of the pyrene-labeled actin in various concentrations. Top scheme: Green arrow describes potential incorporation of G-actin monomer into F-actin filament, and red its dissociation. Schematic representation of nucleation, elongation, and steady-state phase of actin filament assembly based on 1μM actin. Right: distribution of actin polymerization rates pero condition calculated based on Doolittle et al. 2013. (c,d) Left: actin assembly activities of various concentrations of the two splice variants of the DAAM1 FH2-COOH fragment using 0.5 μM (c) and 1 μM actin (d). Actin assembly was measured by incubation of the pyrene-labeled actin. Right: distribution of actin polymerization rates pero condition calculated based on Doolittle et al. 2013.

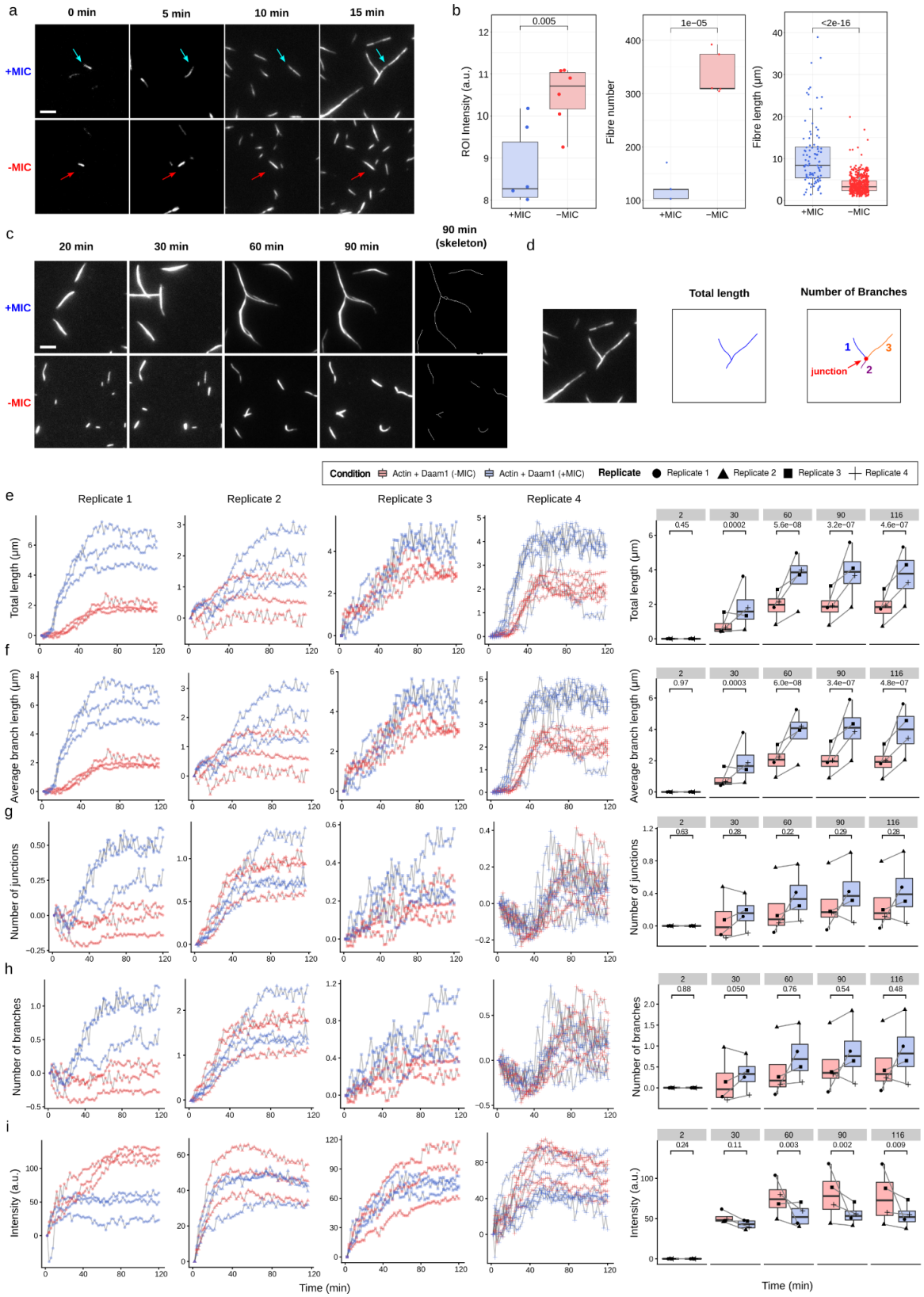
a
0 min
5 min
10 min
15 min
+MIC
-MIC
b
0.005
1e−05
<2e-16
ROI Intensity (a.u.)
Fibre number
Fibre length (µm)
+MIC
−MIC
c
20 min
30 min
60 min
90 min
90 min (skeleton)
d
Total length
Number of Branches
junction
Condition
Actin + Daam1 (-MIC)
Actin + Daam1 (+MIC)
Replicate
Replicate 1
Replicate 2
Replicate 3
Replicate 4
e
Total length (µm)
f
Average branch length (µm)
g
Number of junctions
h
Number of branches
i
Intensity (a.u.)
Time (min)

Supplementary Figure 2 - TIRF microscopy of actin polymerization. (a) Magnification of the actin fluorescence micrographs shown in Figure 2g used for tracking the behavior of individual actin fibers over time (examples indicated by the colored arrows). Scale bar: 2 µm. (b) Quantifications of ROI intensity, fiber number and length from (Figure 2g) at the last recorded time point (15 min). Each dot in the ROI intensity boxplots corresponds to a randomly selected ROI. P-values from Wilcoxon rank-sum tests. (c) Magnification of actin fluorescence TIRF images obtained using 0.2 µM actin and 200nM FH2-COOH Daam1 fragments. The right panels show the skeletonized actin fibers (90 min skeleton) as obtained using the AnalyzeSkeleton Fiji plugin (Schindelin et al. 2012; Polder et al. 2010). Scale bar: 2 µm. (d) Schematic representation of the morphological features analyzed in (e-h). (e-i) Temporal quantifications of F-actin fiber features including fiber total length in µm (e), average length of individual branches in µm (f), number of junctions per object (g), number of branches per object (h), and actin fiber intensity (i). Left: each line describes a different region analyzed in each experimental replicate. Right: Boxplots summarizing the average values of the different F-actin fiber features quantified. Black lines in the box plots connect data points acquired simultaneously during each experimental replicate. P-values from two-way ANOVA tests with replicates as factors.

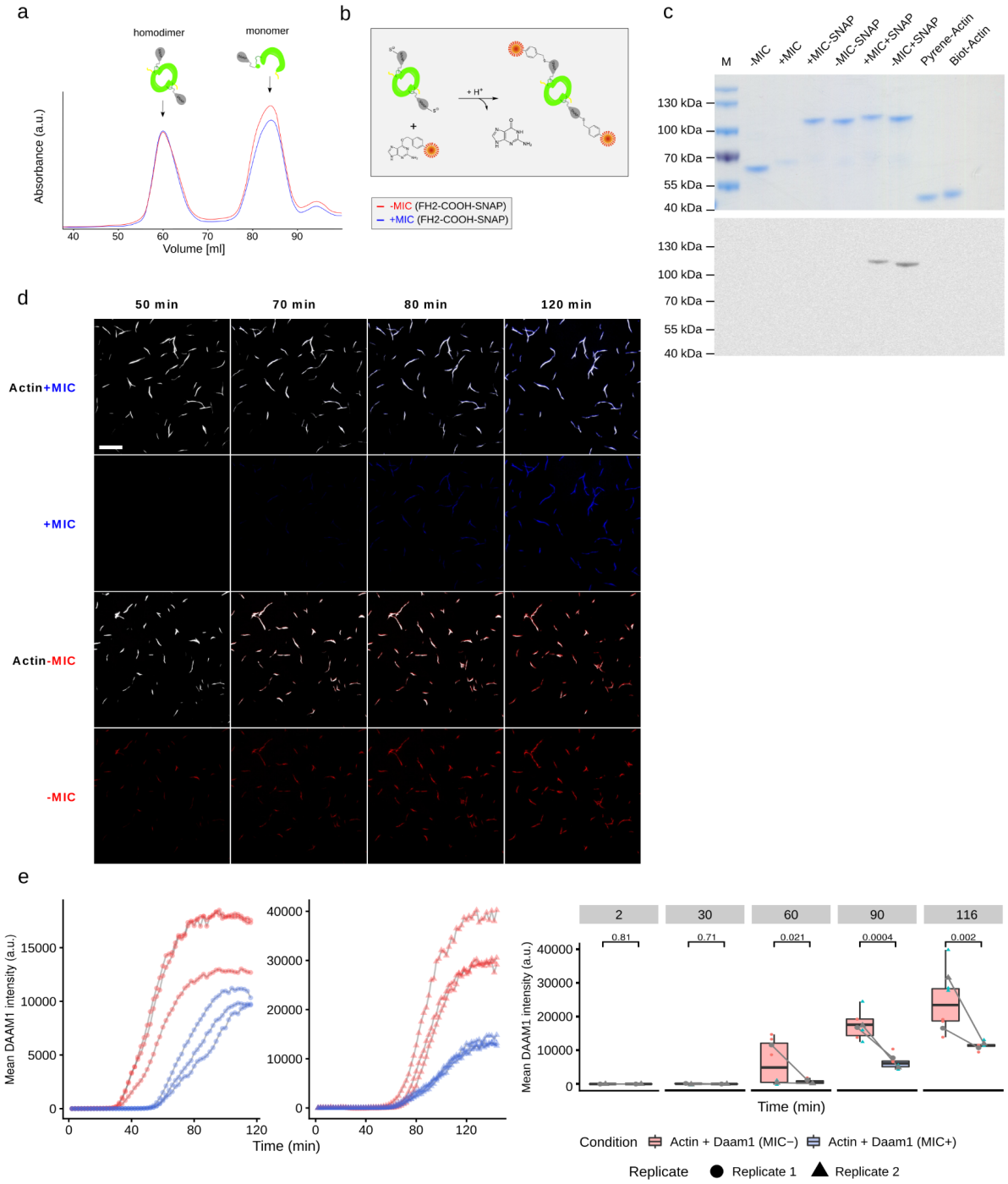

Supplementary Figure 3 - Dual-color TIRF microscopy with SNAP labeling. (a) FPLC elution profiles of DAAM1 SNAP-FH2-COOH fragments purified from bacteria. FPLC was performed using a HiLoad® 16/600 Superdex® 200 pg column. (b) Schematic representation of fluorescence labeling of purified SNAP-FH2-COOH fragments. Green indicates the DAAM1 fragment, gray the SNAP tag, and orange the fluorescent labeling of SNAP tag with Alexa Fluor 488. (c) Top: Coomassie blue-stained SDS-PAGE gel showing all the proteins used throughout the course of this study. Bottom: Fluorescence image of the SDS-PAGE gel, shown in top panel, using blue light excitation. (d) Representative micrographs of dual-color TIRF experiments performed using 0.2 µM actin and 200 nM SNAP-tagged proteins. Scale bar: 10 µm. (e) Quantification of the mean protein fluorescence intensity per actin fiber throughout the course of the experiment. Data plots show multiple regions analyzed per each experimental replicate and boxplots summarize their averages. Gray lines represent the relationship between the protein isoforms in experimental replicates. P-values from two-way ANOVA tests with replicates as factors.

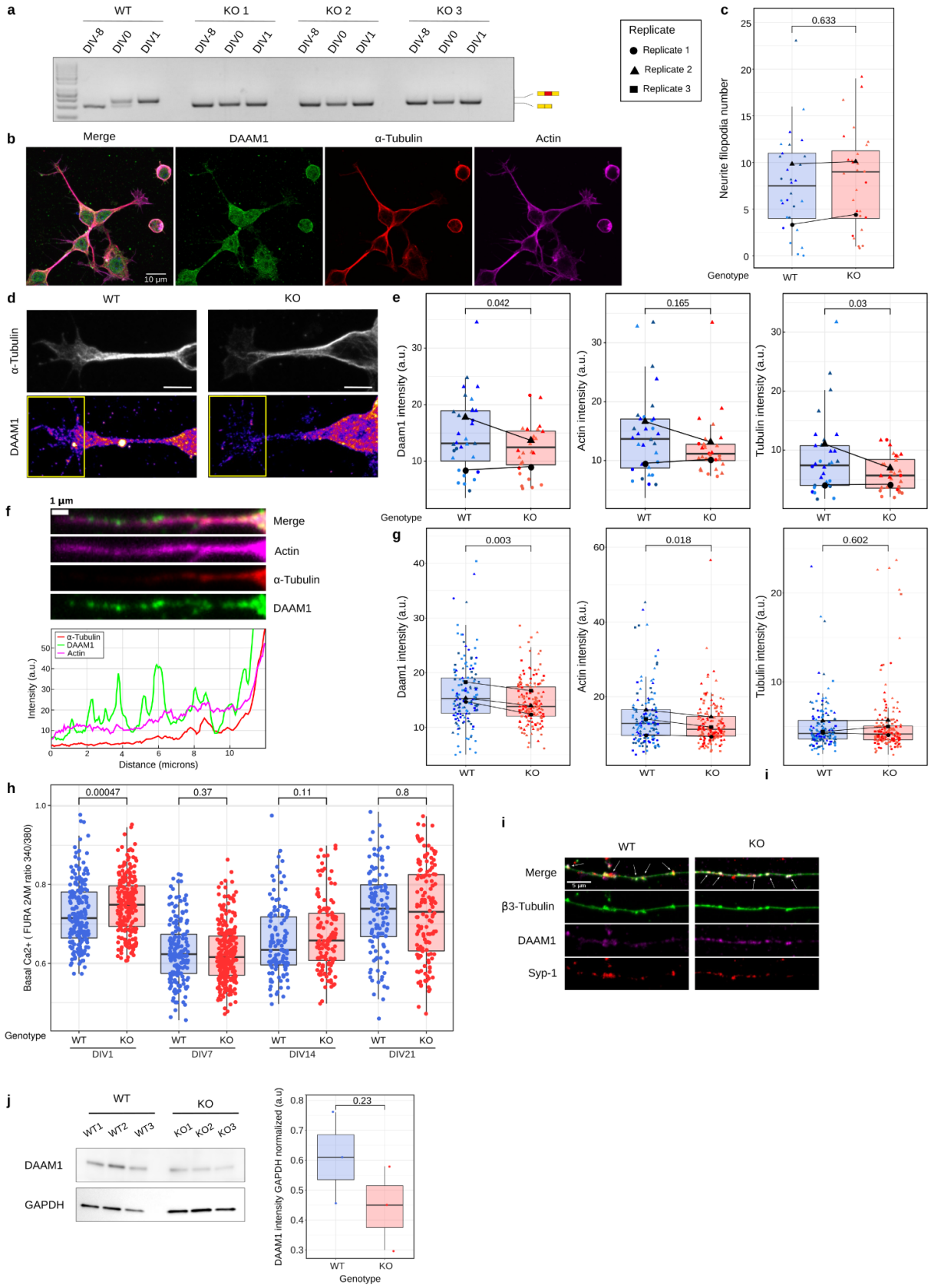
a
WT
KO 1
KO 2
KO 3
DIV-8
DIV0
DIV1
Replicate
Replicate 1
Replicate 2
Replicate 3
b
Merge
DAAM1
α-Tubulin
Actin
10 µm
c
0.633
Neurite filopodia number
Genotype
WT
KO
d
WT
KO
α-Tubulin
DAAM1
e
0.042
0.165
0.03
Daam1 intensity (a.u.)
Actin intensity (a.u.)
Tubulin intensity (a.u.)
f
1 µm
Merge
Actin
α-Tubulin
DAAM1
Intensity (a.u.)
Distance (microns)
g
0.003
0.018
0.602
h
0.00047
0.37
0.11
0.8
Basal Ca2+ (FURA 2AM ratio 340/380)
DIV1
DIV7
DIV14
DIV21
i
β3-Tubulin
Syp-1
5 µm
j
WT1
WT2
WT3
KO1
KO2
KO3
GAPDH
0.23
DAAM1 intensity GAPDH normalized (a.u)

Supplementary Figure 4 - Increased filopodia and neurite length upon microexon removal in neuronal precursors. (a) RT-PCR assays of Daam1-MIC inclusion during neuronal differentiation in WT and KO cell lines. (b) Representative immunocytochemistry image of WT neuronal precursors (NPCs; DIV0+4h). Scale bar: 10 µm. (c) Distributions of neurite filopodia number in NPCs (DIV0+4h). Dots represent values measured on an individual neurite. (d) Representative immunocytochemistry images of derived growth cones from WT and KO NPCs (DIV0+4 h). Relative intensity throughout the last 5 µm of the growth cone (yellow boxes) were analyzed. (e) Distributions of relative intensities of DAAM1, actin and tubulin. Dots represent individual values per growth cone. (f) Top: representative immunocytochemistry images of a filopodia from a WT NPC (DIV0+4 h). Bottom: Intensity spectra throughout the filopodia. (g) Distributions of relative intensities of DAAM1, actin and tubulin. Dots represent values measured on the last 5 µm from the tip of individual filopodia. (h) Basal calcium flux comparison between WT and KO cell lines, based on FURA 2AM ratio throughout the time-course of neuronal differentiation protocol. (i) Representative immunocytochemistry image of a DIV21 neuronal protrusion stained with **β**3-Tubulin, DAAM1 and synaptic marker Syp-1. Arrows highlight overlap between DAAM1 and Syp-1 puncta. (j) Western blot (left) and associated quantification (right) of the relative intensity of DAAM1 normalized to GAPDH. Protein extract from neuronal cultures DIV21. Dots represent values measured on individual cell lines. P-values from Wilcoxon rank-sum tests (h), two-way ANOVA tests with replicate and genotype as factors (c,e,g), or Student's t test (j).

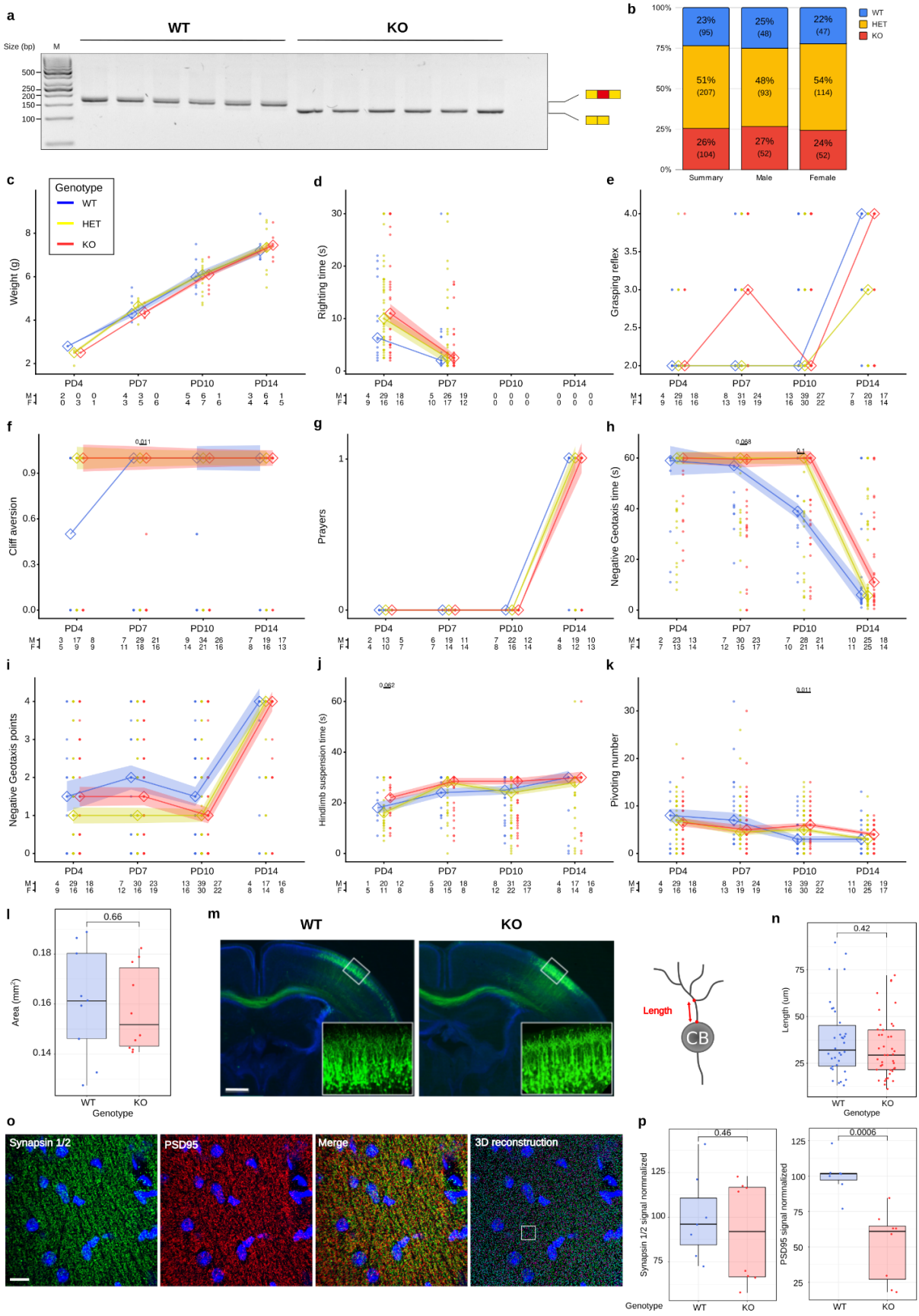
a
WT
KO
Size (bp)
M
500
250
200
150
100
b
100%
75%
50%
25%
0%
23% (95)
51% (207)
26% (104)
25% (48)
48% (93)
27% (52)
22% (47)
54% (114)
24% (52)
Summary
Male
Female
WT
HET
KO
c
Genotype
WT
HET
KO
Weight (g)
PD4
PD7
PD10
PD14
d
Righting time (s)
e
Grasping reflex
f
Cliff aversion
0.011
g
Prayers
h
Negative Geotaxis time (s)
0.058
0.1
i
Negative Geotaxis points
j
Hindlimb suspension time (s)
0.052
k
Pivoting number
0.011
l
0.66
Area (mm²)
WT
KO
Genotype
m
WT
KO
Length
CB
n
0.42
Length (um)
Genotype
o
Synapsin 1/2
PSD95
Merge
3D reconstruction
p
0.46
Synapsin 1/2 signal normalized
0.0006
PSD95 signal normalized
Genotype

Supplementary Figure 5. Results from various neonatal experiments. (a) RT-PCR assays of Daam1-MIC inclusion in WT and KO mice at postnatal day (PD) 21. (b) Distribution of Mendelian ratios for all mice used in this study (N = 406). Numbers in brackets represent the animal number. (c-k) Lineplot representation of the animal weight (c) or performance in various tests (d-k) during the experimental time course (see Supplementary Methods and Figure 4a for details). Thick lines represent mean performance for both sexes, shading represents the standard error mean (SEM). Bottom numbers represent the number of males (M) and females (F) used. Dots represent values measured per animal. P-values from Wilcoxon rank-sum tests against the WT. (l) Quantification of dentate gyrus size across images. One dot represents one animal, where an average of 3 to 6 sections of coronal view of the hippocampus were analyzed. P-values from two-way ANOVA with replicate and genotype as factors. (m,n) Representative images of the neuronal complexity (m), and the quantification of the primary dendrite length (n) as a complexity measurement derived from Kawabata Galbraith et al. 2018. CB corresponds to the cell body. P-values from Wilcoxon rank-sum tests. (o) Representative images of Synapsin 1/2 (presynaptic), PSD95 (postsynaptic) markers and 3D Imaris reconstruction of the merged images from the CA1 hippocampal region of a PD22 control mouse. (p) Distributions of the percentage of Synapsin 1/2 and PSD95 signal normalized to the control mean. P-values from Wilcoxon rank-sum tests.

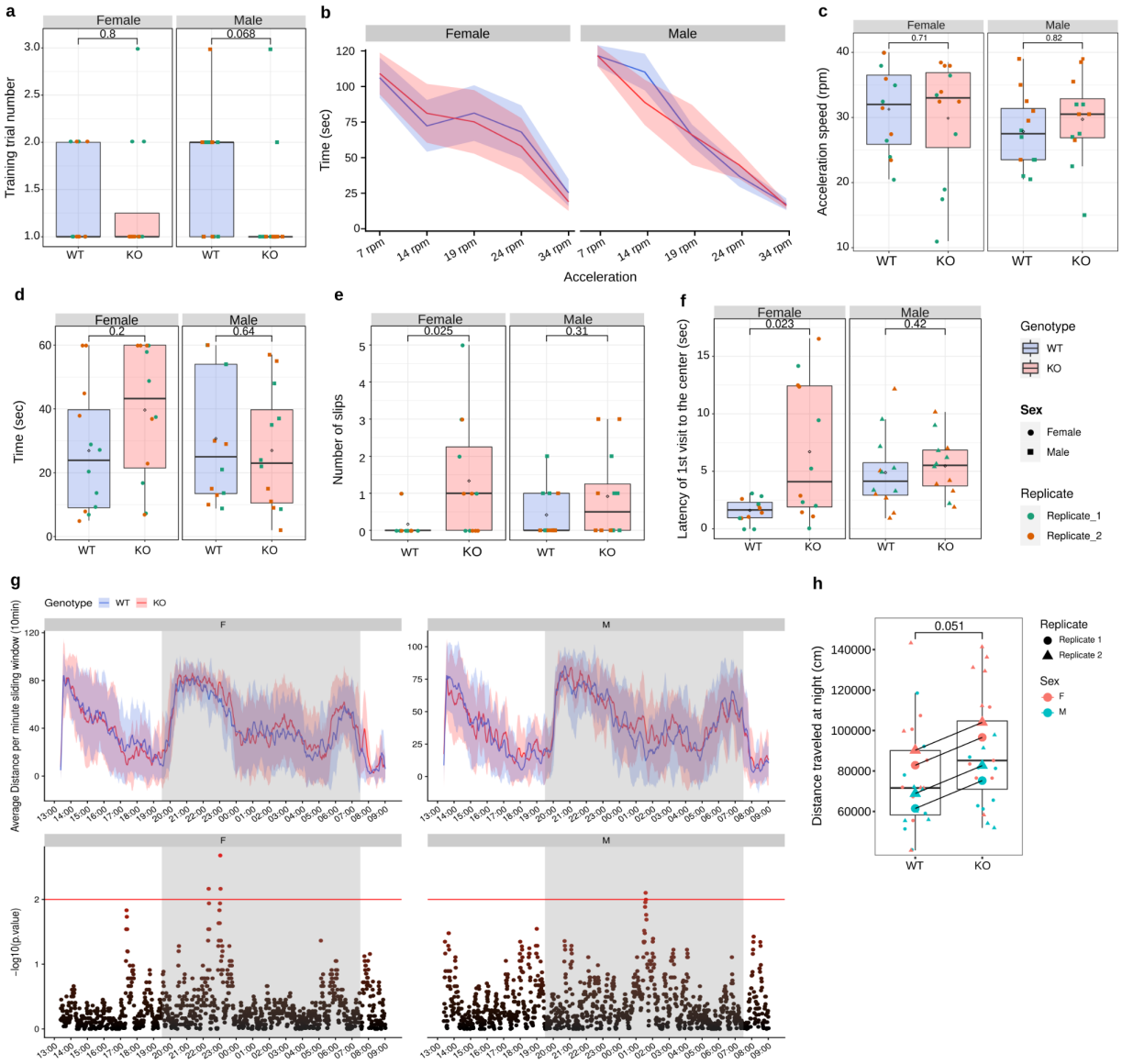

Supplementary Figure 6. Activity, motor coordination and balance tests in adult mice. (a-c) Rotarod performance analysis with training trial number needed to perform the task (a), time based performance during the constant speed sessions (b), and performance during the acceleration session (c). (d,e) Time needed to perform the beam balance task (d) and number of slips from the beam per animal (e). (f) Latency for the entrance to the central zone of the plus-maze. (g) Spontaneous locomotor activity of WT and KO animals during a continuous 23 h period. Top: Average distance traveled per genotype in 10 min (sliding window of 1 min). Bottom: log10 p-value for each 10 minute interval, calculated through permutation tests. The horizontal red line describes the significance threshold, gray area marks light off/dark phase of the night cycle. X-axis describes time and corresponds to the 24 h notation in the form hh: mm. (h) Distance traveled for WT and KO mice during the 12h night period (lights off). P-values from Wilcoxon rank-sum tests (a-f) and two-way ANOVA tests with replicate and genotype as factors (h).

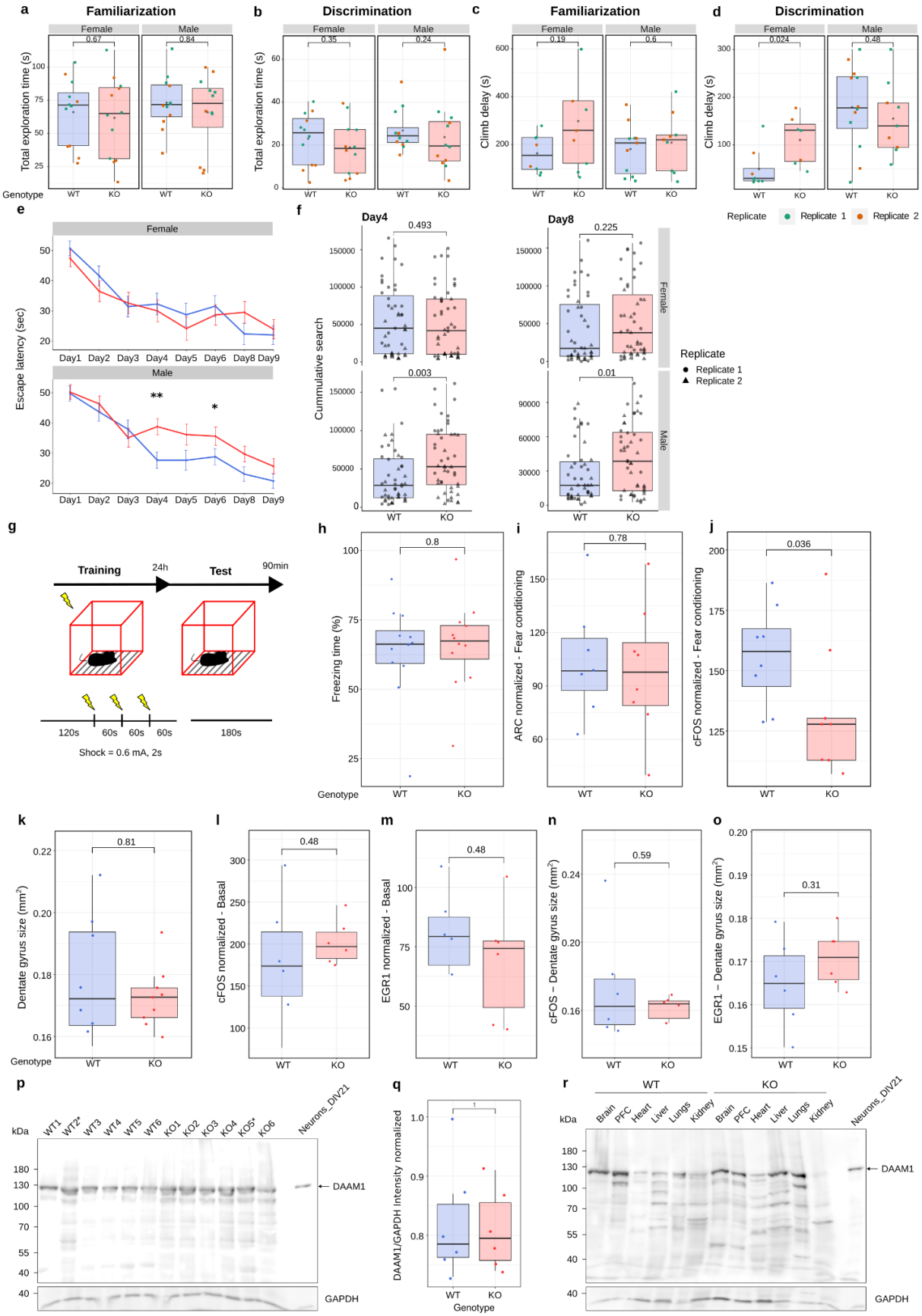
a
Familiarization
Female
Male
0.67
0.84
Total exploration time (s)
Genotype
WT
KO
b
Discrimination
0.35
0.24
c
Familiarization
0.19
0.6
Climb delay (s)
d
Discrimination
0.024
0.48
Replicate
Replicate 1
Replicate 2
e
Escape latency (sec)
Day1 Day2 Day3 Day4 Day5 Day6 Day8 Day9
**
*
f
Day4
Day8
0.493
0.225
0.003
0.01
Cummulative search
Female
Male
Replicate
Replicate 1
Replicate 2
g
Training
24h
Test
90min
120s
60s
60s
60s
180s
Shock = 0.6 mA, 2s
h
0.8
Freezing time (%)
i
0.78
ARC normalized - Fear conditioning
j
0.036
cFOS normalized - Fear conditioning
k
0.81
Dentate gyrus size (mm²)
l
0.48
cFOS normalized - Basal
m
0.48
EGR1 normalized - Basal
n
0.59
cFOS – Dentate gyrus size (mm²)
o
0.31
EGR1 – Dentate gyrus size (mm²)
p
kDa
WT1 WT2* WT3 WT4 WT5 WT6 KO1 KO2 KO3 KO4 KO5* KO6
Neurons_DIV21
DAAM1
GAPDH
q
DAAM1/GAPDH Intensity normalized
r
WT
KO
Brain PFC Heart Liver Lungs Kidney
Neurons_DIV21
DAAM1
GAPDH

Supplementary Fig 7. Cognition and memory related tests. (a,b) Total exploration time defined as object sniffing during the familiarization (a) or discrimination (b) phases of the NOR experiment performed. (c,d) Object climb delay during the NOR familiarization (c) or discrimination phase (d). (e) Latency to find the escape route (hidden platform) in seconds during the acquisition phase for females (upper panel) and males (lower panel). (f) Quantification of the cumulative index during the 4th and 8th day of the acquisition phase. Dots represent the performance of one mouse during one trial. (g) Schematic representation of the contextual fear conditioning test performed. (h) Percentage of freezing time during the test phase of the fear conditioning in male mice. (i-k) Quantification of ARC (i) and cFOS (j) positive nuclei in hippocampal dentate gyrus 1.5 h after the fear conditioning test and size of the measured dentate gyrus regions (k). Number of positive nuclei in (i) and (j) was normalized to the dentate gyrus size (k). One dot represents an average of 3-6 coronal views of the hippocampus analyzed per animal. (l-o) Quantification of EGR1 (l) and cFOS (m) positive nuclei in hippocampal dentate gyrus at basal conditions. Number of IEG positive nuclei was normalized to the dentate gyrus size ([n] and [o], respectively). One dot represents an average of 3-6 coronal views of the hippocampus analyzed per animal, performed in males. (p,q) Western blot (p) and associated quantification (q) of DAAM1 protein expression in cerebellum and motor cortex. Asterisk indicates samples derived from male animals. The relative intensity of DAAM1 was normalized to GAPDH. Dots represent values measured on individual cerebellum. (r) Western blot of DAAM1 protein isoforms in multiple tissues. P-values from Wilcoxon rank-sum tests (a-d,h-o,q) and two-way ANOVA tests with replicate and genotype as factors (e,f).

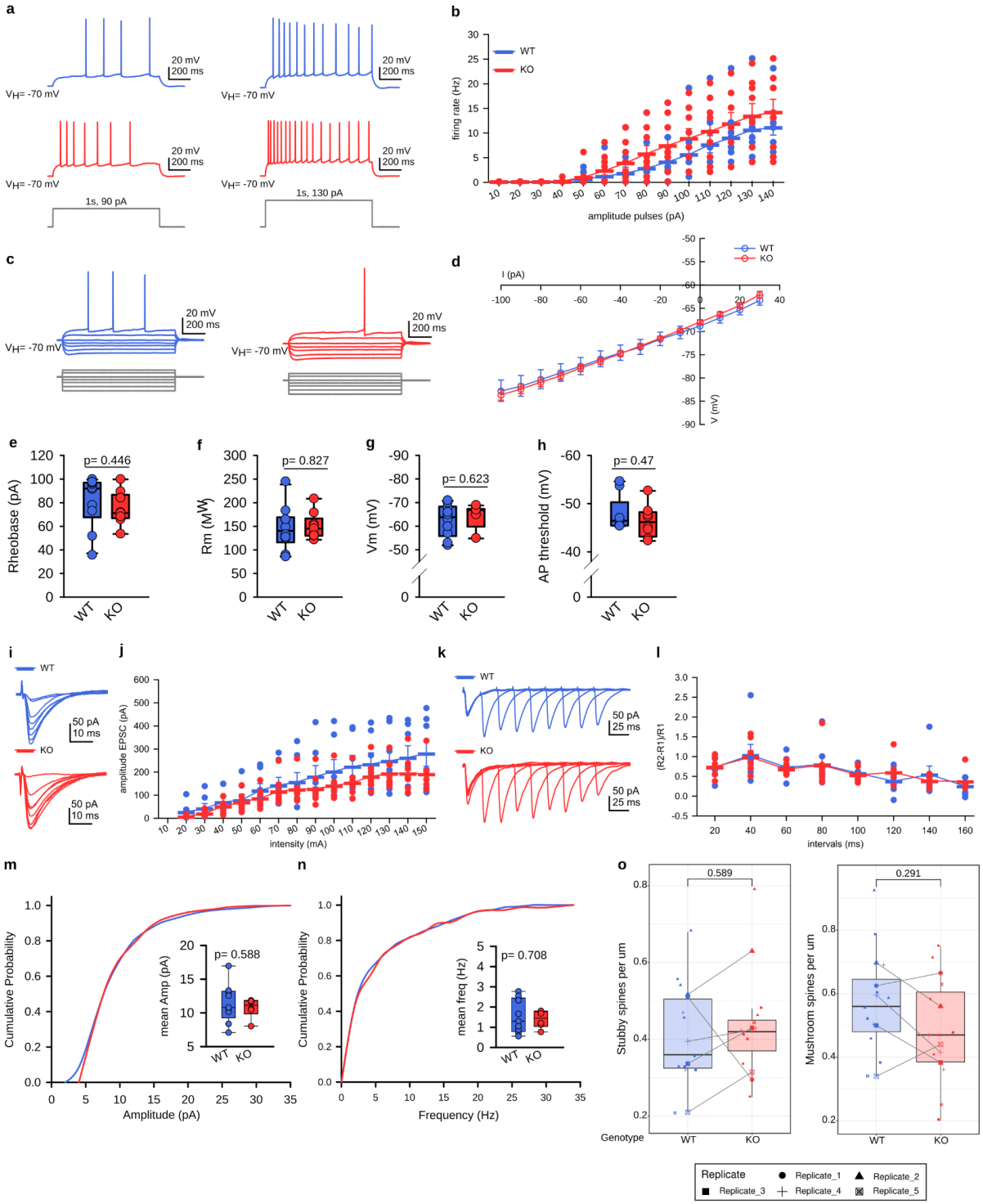
a
20 mV
200 ms
VH= -70 mV
1s, 90 pA
1s, 130 pA
b
WT
KO
firing rate (Hz)
amplitude pulses (pA)
c
d
I (pA)
V (mV)
e
Rheobase (pA)
p= 0.446
f
Rm (MW)
p= 0.827
g
Vm (mV)
p= 0.623
h
AP threshold (mV)
p= 0.47
i
50 pA
10 ms
j
amplitude EPSC (pA)
intensity (mA)
k
50 pA
25 ms
l
(R2-R1)/R1
intervals (ms)
m
Cumulative Probability
Amplitude (pA)
mean Amp (pA)
p= 0.588
n
Frequency (Hz)
mean freq (Hz)
p= 0.708
o
Stubby spines per um
Mushroom spines per um
0.589
0.291
Genotype
Replicate
Replicate_1
Replicate_2
Replicate_3
Replicate_4
Replicate_5

Supplementary Figure 8. Intrinsic membrane properties and release of presynaptic neurotransmitter in CA1 pyramidal cells. (a) Representative traces of action potential firing frequency induced by depolarizing current steps at 90 pA (left) and 130 pA (right) (1s duration) in WT (blue traces) and KO (red traces) cells. (b) Average of the firing frequency versus injected current relationship for representative WT and KO cells. No statistically significant differences found by two-way repeated measures ANOVA tests (WT: n= 10, N= 4; KO: n= 9, N= 4). Error bars indicate SEM. (c) Voltage responses of representative WT (blue traces) and KO (red traces) cells to hyperpolarizing and depolarizing current steps. (d) V/I curves of WT (blue circles) and KO (red circles) cells. Voltage (V) measures in response to hyperpolarizing and depolarizing current (I) steps (WT: n= 10, N= 4; KO: n= 9, N= 4). Error bars indicate SEM. (e-h) Box plots of rheobase (Rh, [e]), membrane resistance (Rm, [f]), resting membrane potential (Vm, [g]) and threshold action potential (th AP, [h]). P-values from Welch's t-test (e, f) and Mann-Whitney (g, h). (WT: n= 10, N= 4; KO: n= 9, N= 4). (i) Example evoked EPSC traces by stimulation of the SC pathway applying different intensities (pA) in WT (top, blue traces) and KO (bottom, red traces) CA1 cells. (j) EPSC amplitude values for a given range of stimulus intensities in WT (n = 7, N= 3) and KO (n = 8, N= 3) cells.No statistically significant differences found by two-way repeated measures ANOVA tests. Error bars indicate SEM. (k) Representative pair of evoked EPSC traces for different intervals (ms) of stimulation of the SC axons in WT (top, blue traces) and KO (bottom, red traces) CA1 cells. (l) Paired-pulse ratios calculated from EPSC amplitudes ((R2-R1)/R1, where R1 corresponds with the first response and R2 second response) across varying inter-stimulus intervals showed unchanged facilitation between WT (n = 7, N= 3) and KO (n = 8, N= 3) cells. No statistically significant differences found by two-way repeated measures ANOVA. Error bars indicate SEM. (m,n) Cumulative probability plot and box plot of amplitude (m) and frequency (n) isolated miniature EPSC events recorded in pyramidal cells in WT (n= 9, N= 3, Events= 1703) and KO (n= 6, N= 3, Events= 1040) CA1 cells. (o) Number of stubby (left) and mushroom (right) spines per 1 µm of neurite from biocytin stained CA1 pyramidal neurons of the hippocampus in WT and KO mice. N = 6 mice for each genotype, 100 µm of dendrites per cell. One dot represents one neuron analyzed. Lines represent the relation between animals analyzed in experimental replicates. P-values from Wilcoxon rank-sum tests.

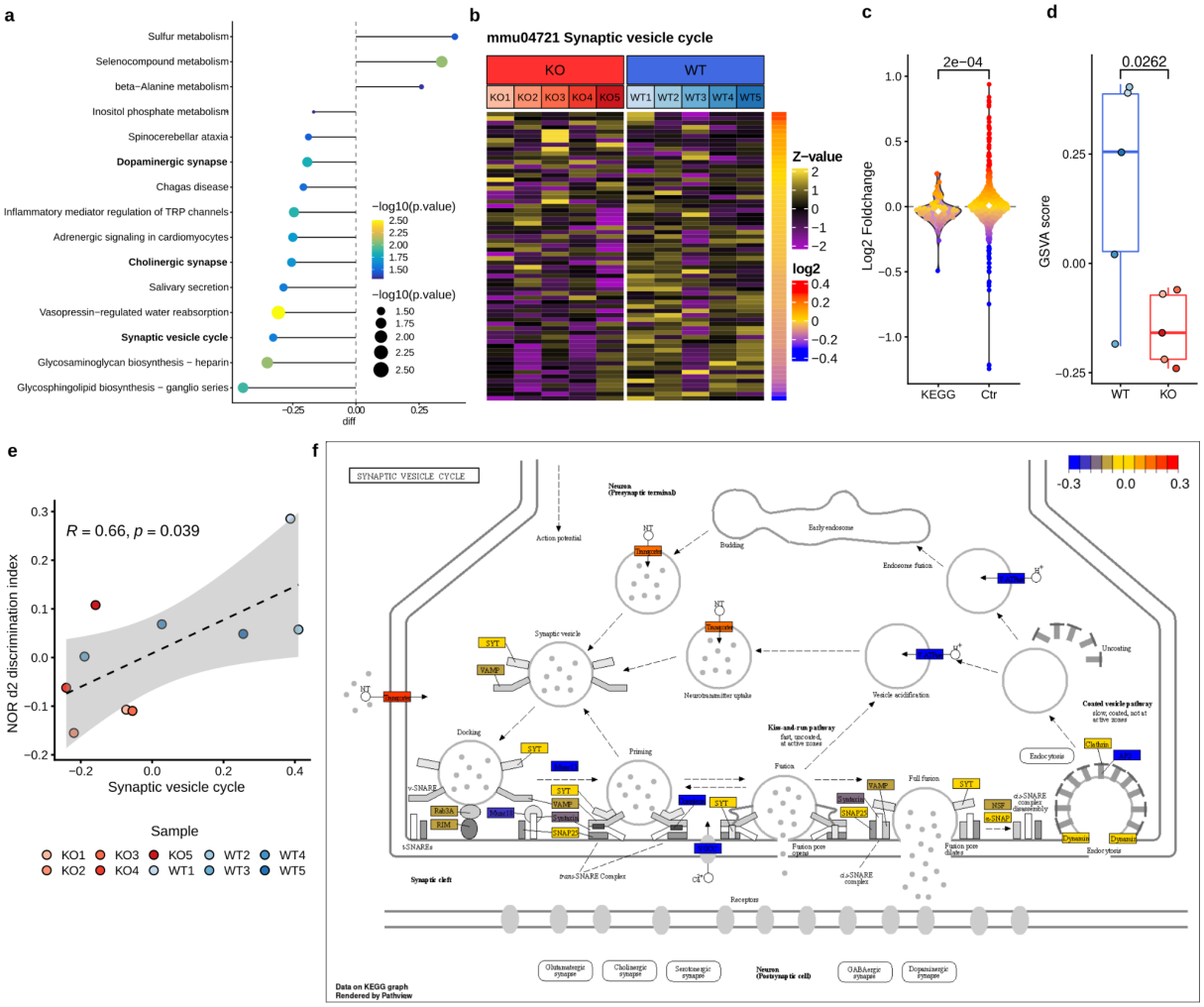

Supplementary Figure 9. Impaired synaptic vesicle cycle upon Daam1-MIC removal. (a) KEGG pathways differentially expressed (p-value < 0.05 of a linear regression on the GSVA-score testing for genotype) are shown in y-axis. X-axis represents the difference between means of KO and WT GSVA-score, with color and size representing -log10(p-value). (b) Expression z-score for genes from the "Synaptic vesicle cycle" KEGG term (mmu04721) sorted by combined shrinked log2 fold change (heatmap in the right column) in the ten RNA-seq samples. (c) Violin plots showing log2 fold change distributions of all genes in the synaptic vesicle cycle pathway compared to a random sample of 1000 genes outside the selected pathway. P-value corresponds to the mean p-value of two-sided Wilcoxon rank-sum tests against 100 random sampling. Points are colored based on log2 fold change. (d) GSVA score per individual hippocampi. P-value from a general linear model comparing WT and KO mice. (e) Pearson correlation between NOR discrimination index d2 and the RNA-seq derived GSVA values for the synaptic vesicle cycle genes (b). (f) KEGG pathway for the synaptic vesicle cycle where elements are colored based on shrinked Log2 fold change between WT and KO mice.

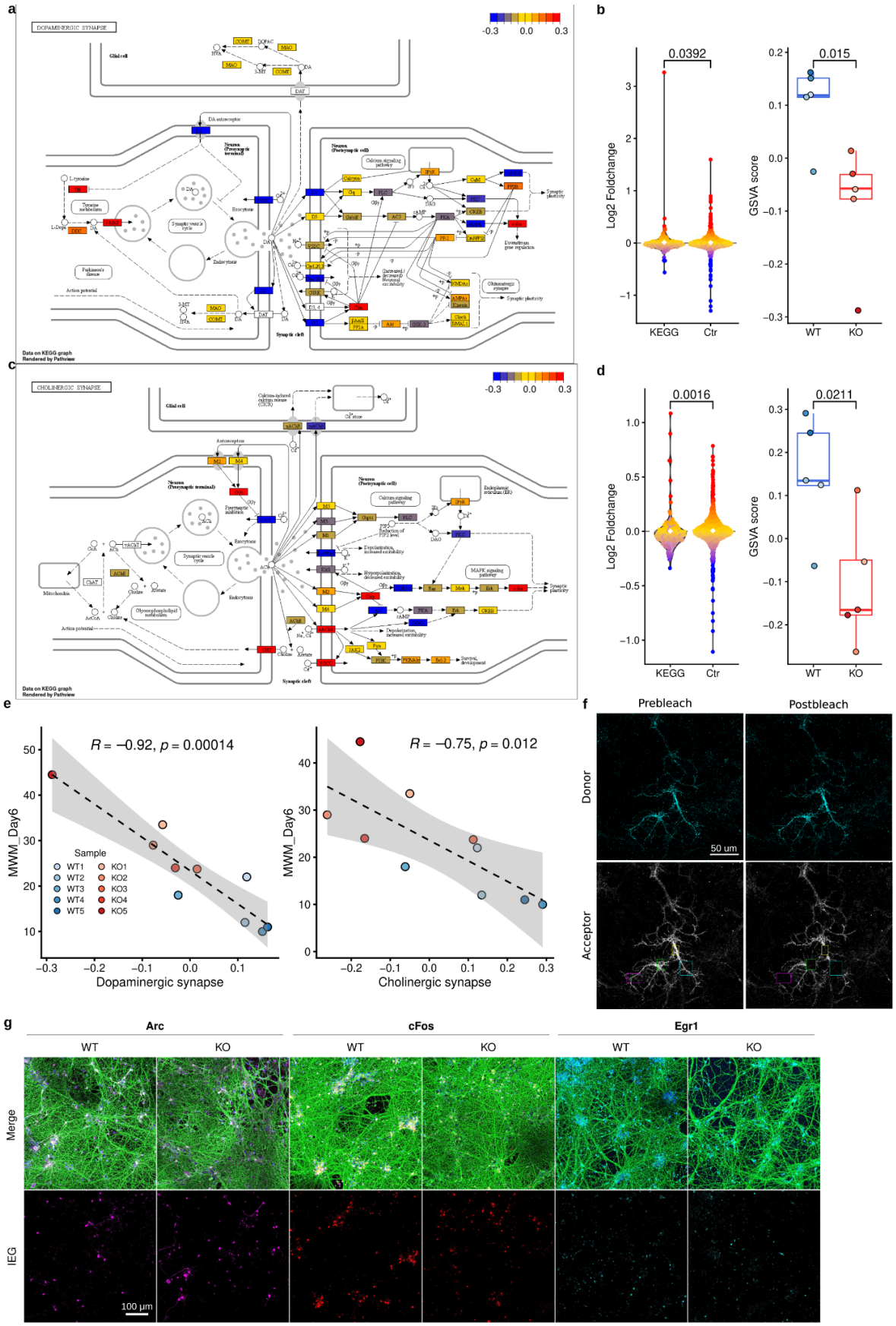
a
DOPAMINERGIC SYNAPSE
-0.3 0.0 0.3
Data on KEGG graph
Rendered by Pathview
b
0.0392
0.015
Log2 Foldchange
GSVA score
KEGG
Ctr
WT
KO
c
CHOLINERGIC SYNAPSE
-0.3 0.0 0.3
Data on KEGG graph
Rendered by Pathview
d
0.0016
0.0211
Log2 Foldchange
GSVA score
KEGG
Ctr
WT
KO
e
R = −0.92, p = 0.00014
R = −0.75, p = 0.012
MWM_Day6
Sample
WT1
WT2
WT3
WT4
WT5
KO1
KO2
KO3
KO4
KO5
Dopaminergic synapse
Cholinergic synapse
f
Prebleach
Postbleach
Donor
Acceptor
50 um
g
Arc
cFos
Egr1
WT
KO
Merge
IEG
100 µm

Supplementary Figure 10. Other KEGG synaptic pathways and molecular phenotypes. (a-d) Representation of the KEGG "Dopaminergic synapse" (mmu04728, [a]) and "Cholinergic synapse" (mmu04725 and, [c]), where each element is colored based on shrinked log2 fold change between WT and KO mice. Violin plots (b,d; left) show the corresponding log2 fold change distribution of all genes in these pathways compared to random samples of 1000 genes outside the selected pathways. P-value corresponds to the mean p-value of two-sided Wilcoxon rank-sum tests against 100 random sampling. Points are colored based on log2 fold change. Boxplots (b,d; right) show the GSVA score per hippocampi RNA-seq sample for the corresponding pathway. P-value from a general linear model comparing WT and KO mice. (e) Pearson correlation between the Morris Water Maze performance during day 6 and the RNA-seq GSVA for the Dopaminergic (left) and Cholinergic synapse genes (right). (f) Representative images of RhoA2G acceptor photobleaching in differentiated neuronal cells (DIV21). (g) Immunocytochemistry for ARC, cFOS and EGR1 positive nuclei in glutamatergic neurons (DIV21). Merge corresponds to IEG, **β**3-Tubulin and DAPI staining overlap. Scale bar 100 µm.

Supplementary Tables

Supplementary Table S1

Name	Sequence	Purpose
Mmu Daam1 F	CCTTGAAGACCTAGAAAGAACGTTC	RT-PCR
Mmu Daam1 R	GAAGGATGTTGCAATTCTGAGCTC	
Dre daam1a F	TGGATCTGGACGACGTCAGAG	
Dre daam1a R	GAAGTGACAGTGTCGTCCTCG	
Daam1_1u_F	CACCGGTGGTGCAGGACAAAAGGGC	CRISPR/Cas9 Genome editing
Daam1_1u_R	AAACGCCCTTTTGTCCTGCACCACC	
Daam1_1d_F	CACCGTTAGCTAACAAGATAACCAA	
Daam1_1d_R	AAACTTGGTTATCTTGTTAGCTAAC	
Daam1_gF	CCCACTTGAAATGGTGTGGAG	Genotyping
Daam1_gR	AGAACCATGGGGCTAAACGA	

Supplementary Table S2

	Stain	Catalog nº	Supplier
Primary antibody	Synaptophysin 1	101004	Synaptic Systems
	DAAM1	14876-1-AP	Proteintech
	Arc (C-7)	sc-17839	Santa Cruz biotechnology
	β-3 Tubulin (TUBB3)	PRB-435P	BioLegend
	α-Tubulin (DM1A)	3873	Cell signaling
	cFos	226004	Synaptic Systems
	PSD-95	ab192757	Abcam
	Synapsin 1/2	106002	Synaptic Systems
Secondary antibody	anti-Rabbit IgG – Alexa Fluor 488	A-11034	ThermoFisher Scientific
	anti-Guinea Pig IgG – Alexa Fluor 555	A-21435	ThermoFisher Scientific
	anti-Mouse IgG – Alexa Fluor 594	A-11005	ThermoFisher Scientific
	anti-Rabbit IgG – Alexa Fluor 647	A-21443	ThermoFisher Scientific
	anti-Rabbit IgG – Alexa Fluor 488	A-21206	ThermoFisher Scientific
	anti-Mouse IgG – Alexa Fluor 647	A-31571	ThermoFisher Scientific
	Rabbit Anti-Goat IgG H&L (HRP)	ab6741	Abcam
Reagent	Phalloidin-iFluor 647	ab176759	Abcam
	SiR-Actin	CY-SC001	Spirochrome
	Fast Green FCF	F7252	Merck
	Fluoroshield™ with DAPI	F6057-20ml	Merck

Supplementary Methods

Mouse embryonic stem cell culture

mESC were grown on 0.1% gelatine-coated (Millipore, ES-006-B) plates (Thermo Scientific Nunc Cell-Culture Treated Multidishes, 140675) with mESC media containing 10% fetal bovine serum (FBS) and leukaemia inhibitory factor (LIF). Gelatine coating was performed for a minimum of 5 minutes before plating the cells. mESC media was generated by the CRG Tissue Engineering Unit and consisted of: Glasgow's Minimum Essential Medium (GMEM) BHK-21 (Gibco, 21710-025) supplemented with 10% fetal bovine serum (Seralab, A1060013 EU-000-H), Minimum Essential Medium non-essential amino acids solution (Gibco,11140-050), 1mM L-Glutamine (Gibco, 25030-024), 0.5mM Sodium Pyruvate (Gibco, 11360-070), 0.1mM 2-Mercaptoethanol (Millipore, ES-007-E) and recombinant mouse LIF protein 1000U/ml ESGRO (Millipore, ESG1107). mESCs were routinely passaged using 1x TrypLE Express Enzyme (Gibco, 12605028).

Neuronal differentiation

We followed the protocol reported by Bibel et al., 2007 with slight modifications. In brief, mESCs were harvested by trypsinization with TrypLE Express for 5 min at 37°C (HeracellTM 240i CO2 Incubator). Trypsin was quenched with an equal volume of Embryoid Body (EB) medium (10% FBS, 1% Non-Essential Amino Acids, 1% Penicillin and Streptomycin, 1% GlutaMax, 1% Sodium Pyruvate, 0.1% B-mercaptoethanol, 86% DMEM High Glucose) and cells were counted manually using a haemocytometer chamber. mESCs were plated at a density of 4x106 cells per low attachment bacteriological petri dish (10 cm Ø) in 15 ml of EB medium. This marks the start of the experiment and is further referred to as Day In Vitro -8 (DIV-8). Cells were cultured at 37°C with 5% CO2. On day 2 medium with the Embryoid Bodies (EB) was transferred to the falcon tube, and after 5 min supernatant was aspirated and pelleted EBs were resuspended in fresh EB medium (DIV-6). Resuspended EBs were dispensed into new bacteriological Petri dishes (10 cm diameter) in EB medium volume up to 15 ml per dish, and incubated as earlier. On day 4 (DIV-4) and day 6 (DIV-2) the medium was changed as before but using EB medium supplemented with 5 µM retinoic acid. On day 8 (DIV0) EBs were collected as before and washed twice with 10 ml of PBS. Subsequently, EBs were resuspended in 1 ml of medium (0.05% Trypsin, 0.05% EDTA dissolved in PBS) and incubated with constant shaking for 3 min in a 37°C water bath. Trypsinized EB's were quenched with 1 ml of EB medium and cells were pelleted down using Eppendorf 5810R Centrifuge (180 g for 5 min). The supernatant was aspirated and the cells were resuspended in 5 ml of N2 medium and filtered through a 40µm cell strainer. The cells were counted as before and plated at the density of 1.5x105 per 13 mm glass coverslip (VWR 631-1578) placed in 24 well plates (Sigma Aldrich, 11243217001) coated with poly-D-Lysine followed by laminin (Roche). Cells were cultured as described above in the incubator set up at 37°C with 5% of CO2. After 2, 24 and 48 h from plating, the N2 medium was changed. Consecutively, media was changed to B27 after 72 h and fresh B27 media was provided every second day. Neuronal differentiation was conducted up to DIV23.

Behavioral and locomotor tests in a neonatal mice

A battery of behavioral and motor tests to probe early post-natal neurodevelopment was performed as described in Feather-Schussler and Ferguson (2016) and Roper et al. 2021, with some adjustments. In particular, we performed tThe following tests were performed at PDs 4, 7, 10 and 14, unless stated otherwise:

Pivoting and walking: Pivoting is a voluntary exploratory behavior displayed by young mice before the forward locomotion. To measure pivoting, mice were placed on a flat surface and allowed to move freely for 1 min. The number of times the animals made a 90° turn was recorded. Pivoting was measured based on the body axis with the help of a cross marking 90° angles on the experimental surface. The latency to walk in a straight line after the end of the pivoting behavior was also measured. Two trials were performed per animal.

Righting reflex: Mice (PD4 or PD7) were placed on their back on a padded table top. The time taken for the animals to right themselves back to four paws through 180° was measured for a maximum of 1 min. The direction of turning was also recorded. The experiment was performed three times per animal and the mean calculated.

Preyer's reflex: The Preyer's reflex is a startle response triggered by sharp auditory stimuli and is used to assess hearing in rodents (Jero, Donald E. Coling, Anil K. Lal 2001). The experimenter made a sharp clapping sound by stretching and releasing a rubber glove onto the hand in the proximity of the mouse and recorded the presence of rapid whole-body movement.

Front-limb suspension: To measure forelimb strength, mice were allowed to grasp with both forepaws on a horizontal bar suspended above a padded drop zone. The latency to fall was measured in three trials per animal and the mean was calculated.

Hindlimb suspension: To measure hindlimb strength, mice were lowered into a 50 ml conical tube and released with their hindlimbs hung over the rim. The latency to fall was measured for up to 30 s. Hindlimb posture upon falling was scored 0-4 based on the limb spread, as described in Feather-Schussler and Ferguson (2016). The experiment was performed only once unless the animal fell down immediately due to bad placement.

Grasping reflex: The animals were held by the scruff of the neck and each paw was touched by a toothpick to elicit the grasping reflex. Performance was scored 0-4, assigning one point per paw in the presence of grasping. Left and right paw preference was also noted.

Cliff aversion: Cliff aversion tests the labyrinth reflexes, as well as normal strength and coordination. Mice were placed on top of a box elevated ~10 cm above the surface, with their snout and part of their forepaws just over the edge. The presence of aversive movement away from the cliff within the subsequent 30 s was recorded. If the pup fell down, one additional trial was performed.

Negative geotaxis: Negative geotaxis is an automatic vestibular response to geogravitational stimuli and is used to measure motor coordination in pups. Mice were placed head-facing uphill on a plastic platform with an inclination of 45° covered with Surface Protector Paper and spunlace wipes (VWR), except for PD 4 mice, for which the incline was adapted to 30°. After ~5 s, the pups were turned by 180° to face downhill, and their movement was observed for 1 min. Two trials were performed, turning the animal in opposite directions to the start position to avoid left-right bias. Animals were given 0.5 points per 45° of turning. If a full 180° turn was performed, the latency was also recorded. Left and right turning preferences were also noted.

Homing test: Homing was performed as described in Roper et al. 2021 at PD14 with adjustments. A pup is removed from the home cage and is placed in the corner of a new clean cage (12.5 × 45 cm, w × h) facing the wall. The new cage is filled with clean wood shavings, and familiar nesting material from its home cage is provided in the opposite corner. The time for the pup to reach the area containing the nesting material is recorded in seconds, with a maximum time of 2 min.

Spontaneous basal locomotor activity in adult mice

Spontaneous basal locomotor activity during day and night in an open cage was measured for 23 h using an infrared Actimeter (PANLAB SA, Spain). Individual mice were placed in the open field (25 × 25 cm), and their position in time was recorded based on the disruption of infrared beams in the x and y axes. The arena was covered with a layer of wood shavings, and sufficient water and food was provided.

Novel Object Recognition (NOR) test

The NOR test measures recognition memory based on the visual paired-comparison paradigm (Leger et al. 2013; Lueptow 2017). The experiment consists of three sessions carried out on consecutive days: habituation, familiarisation, and discrimination. The experiment was performed in a 38.5 cm × 38.5 cm arena with 38.5 cm high dark plastic walls and an open top. The arena was illuminated from the top, and the animals were tracked using video recording and the Smart 3.0 software (System Motor Activity Record and Tracking, PANLAB SA, Spain). To minimize stressors interfering with the experiment, a curtain was mounted separating the arena from the experimenters. The arena and the objects were cleaned with 70% ethanol between each mouse to remove odors. Cages were transferred to the experimental room 30 min before the trials to acclimatize. The test was carried out under slightly aversive conditions (white light 50 lux).

Habituation: On the first day, animals were placed into the arena facing the wall and were recorded for 5 min. Their movement was measured separately by the Smart 3.0 software in a central (20 × 20 cm) and a peripheral zone.

Familiarization: On the second day, two identical objects (A and B) were placed in the centre of the box, 18 cm apart. Animals were placed into the box facing the wall and were recorded for 10 min. The time spent exploring each object was measured manually using a timer. The latency to climb on top of the objects was also noted. The exploration was defined as the time spent sniffing the object from a close distance, excluding the time spent climbing on the object. Exploration threshold was established at 20 sec.

Discrimination: On the third day, one of the objects was replaced with a novel object of a different shapes and colours. Animals were placed into the box facing the wall as before and were recorded for 5 min. The time spent exploring each object was measured manually using a timer. The latency to climb on top of the old and novel objects was noted.

Discrimination and preference indices were calculated for familiarisation and discrimination for each animal based on the manual exploration time recordings, as described in Lueptow et al. (2017).

Elevated Plus Maze test

Anxiety-related behavior was measured in the Elevated plus maze, as described by (Walf and Frye 2007), with some modifications. The apparatus consisted of a cross-shaped platform with four arms (30 cm × 5 cm), elevated 40 cm off the ground. Two arms were open and two were enclosed by 15 cm high black methacrylate walls. The open arms create an aversive environment for the mouse, while the dark enclosed space of the closed arms is considered safe. The number of open arm entries and the relative time spent in the open arms is indicative of anxiety-related behavior. Animals that avoid open arms are considered more anxious. Mice were lowered onto the end of the same closed-arm facing the walls and their movement was recorded for 5 min using the Smart 3.0 software. Separate zones were set up for each arm, the ends of the arms (5 cm × 5 cm) and the center of the cross (5 cm × 5 cm). Measurements included the percentage of the time, entries, distance traveled, and average speed in each zone. Rearings and head dippings from the central zone were recorded manually. The arena was cleaned with 70% ethanol between each animal's experiment to remove odors.

Morris Water Maze test

Learning and visual-spatial memory were tested in the Morris water maze (Morris 1984), with some modifications (Vorhees and Williams 2006). In this experiment, mice must learn the spatial location of a submerged platform to escape from the water by building a cognitive allocentric map with the help of external visual cues. A metal tank (150 cm in diameter) was filled with water (22-23°C) with added white, non-toxic finger paint to conceal the location of the platform. The platform (12 cm in diameter) was submerged 0.7 cm below the water surface. Four quadrants (NE, NW, SE, SW) and a platform zone were defined using the Smart 3.0 software, with the platform located in the center of one quadrant (NE). A curtain was mounted around the tank to separate it from the experimenters and minimize external visual cues. Three distal visual cues, a square, a triangle and a circle were placed on the curtains around the tank at equal distances, ~30 cm above the water surface. The experiment consists of the following phases: training trials, removal, cued trials, and reversal training.

Training trials: During training, the mice learn the task and the location of the platform. Four 1-min training trials were performed each day, with an inter-trial interval of ~1 h. Nine training days were performed to achieve sufficient learning. Mice were released into the water. The latency to reach the platform was recorded and the animal was removed from the water. 5 to 15 s platform localization learning and positive reinforcement was used by placing the animal on the platform depending on performance (goal accomplishment or lack of it).

Removal: the platform is removed from the tank and the animals are tested for 1 min 24 h after the last training. Animals were released from the location furthest away from the original platform (SW). Mice that remember the location of the platform are expected to spend more time in the platform quadrant (NE).

Cued trials: In these guided learning trials, the platform is placed back to its original location and is marked by a local visual cue. Animals have an inherent tendency to swim towards the flag. Therefore, these trials can detect issues with swimming, visual perception and/or motivation to perform the task. A flag (~10 cm above the water surface) fixed to a metal bar was used as a local cue. Distant visual cues were removed. Two 1-min cued trials were performed ~1 h after the removal session.

Reversal training: During a spatial reversal, the platform is placed opposite to its original location (SW). Mice must flexibly re-learn the spatial location of the platform. Four trials were performed for 2 days, as described in the training trials.

In all trials, the latency to reach the platform and platform crossovers were measured. Animals were tracked using the Smart 3.0 software, allowing measurement of time, speed and distance traveled in each quadrant. Distances from the platform were used to calculate cumulative search error and mean proximity as additional measurements of spatial learning (Pereira & Burwell, 2015). Floating was also measured manually.

Grip strength test

The grip strength experiment is a measurement of neuromuscular function and limb muscle strength. Mice were held by the tail and lowered onto the metal grid of the apparatus (Grip Strength Meter, Bioseb, France), allowing them to grip with their paws. Mice were next pulled backwards along the grid at a consistent speed, while the apparatus measured the force exerted by the animals on the grid. Grip strength was measured for forelimbs through 3 consecutive trials. Best, average, and mean grip strengths were calculated.

Rotarod test

To evaluate coordination and balance, we employed the Rotarod apparatus (PanLab Rotarod LE8200, Spain) based on (Deacon 2013). First, animals were trained to walk on the rod at 4 rpm. Training sessions were performed until the mouse managed to walk on the rod for 1 min. After training, test sessions were performed at five constant speed settings (7, 14, 19, 24, 34 rpm). Two trials were carried out per speed, with a maximum length of 2 min. Finally, two trials were performed where the rotation speed accelerated constantly from 4 to 40 rpm in 60 s.

Beam Balance test

Balance, coordination, and vestibular function were measured in the Beam Balance experiment (Luong et al. 2011). Mice were placed in a standing position in the center of a narrow wooden beam (1 cm × 50 cm) elevated 45 cm above the ground. They were scored 0-3 based on how far they walked on the beam within 1 min (0: falls off; 1: <10 cm; 2: >10 cm; 3: reaches the end). Falls and the number of slips were also recorded, as well as the latency to reach one of the ends and the direction of movement (left/right).

Fear conditioning test

The fear condition test is used to evaluate Pavlovian learning and memory. Experiments are performed in a 30 × 25 × 33cm chamber with grid floors and opaque square ceilings. After each session, the apparatus was cleaned with 70% ethanol. During the light cycle, 10-12 week old male mice were subjected to behavioral trials (7:30 am to 1:00 pm). In three successive days, each mouse was handled and habituated to the investigator for five minutes. Handling took place in a separate room from where the CFC apparatus was. Mice were transferred to the handling room by a wheeled trolley prior to each handling session to familiarize them to the journey. Mice were trained in Context A for 300 s, with three 0.6 mA shocks of 2 s duration delivered at 120 s, 180 s and 240 s, respectively. After training mice were placed back in their home cages and were placed in the holding room. Context A testing session lasted 180 s. Testing conditions were identical to training conditioning, except that no shocks were delivered. At the end of each session, mice were placed in their home cages and carted back to the holding room. Packwin 2.0 software (Panlab, Harvard Apparatus) automatically identified freezing behavior (>800 ms immobility). Every day of the experiment, cages were calibrated in accordance with manufacturer recommendations.